

Azimuthal anisotropy from Eikonal Tomography: example from ambient-noise measurements in the AlpArray network

E.D. Kästle¹, I. Molinari², L. Boschi^{3,4,2}, E. Kissling⁵, and the AlpArray Working Group

¹ *Institute for Geological Sciences, Freie Universität Berlin, Germany*

² *Istituto Nazionale di Geofisica e Vulcanologia, Sezione di Bologna, Italy*

³ *Dipartimento di Geoscienze, Università degli Studi di Padova, Italy*

⁴ *Institut des Sciences de la Terre Paris, Sorbonne Université, CNRS-INSU, ITeP UMR 7193, F-75005 Paris, France*

⁵ *Department of Earth Sciences, ETH Zürich, Switzerland*

SUMMARY

Ambient-noise records from the AlpArray network are used to measure Rayleigh wave phase velocities between more than 150,000 station pairs. From these, azimuthally anisotropic phase-velocity maps are obtained by applying the Eikonal tomography method. Several synthetic tests are shown to study the bias in the Ψ_2 anisotropy. There are two main groups of bias, the first one caused by interference between refracted/reflected waves and the appearance of secondary wavefronts that affect the phase travel-time measurements. This bias can be reduced if the amplitude field can be estimated correctly. Another source of error is related to the incomplete reconstruction of the travel-time field that is only sparsely sampled due to the receiver locations. Both types of bias scale with the magnitude of the velocity heterogeneities. Most affected by the spurious Ψ_2 anisotropy are areas inside and at the border of low-velocity zones. In the isotropic velocity distribution, most of the bias cancels out if the azimuthal coverage is good. Despite the lack of resolution in many parts of the surveyed area, we identify a number of anisotropic structures that are robust: in the central Alps, we find a layered anisotropic structure, arc-parallel at mid-

crustal depths and arc-perpendicular in the lower crust. In contrast, in the eastern Alps, the pattern is more consistently E-W oriented which we relate to the eastward extrusion. The northern Alpine foreland exhibits a preferential anisotropic orientation that is similar to SKS observations in the lowermost crust and uppermost mantle.

Key words: Seismic anisotropy – Seismic interferometry – Seismic tomography – Wave propagation – Continental tectonics: compressional

1 INTRODUCTION

With the availability of very dense seismic network data, array-based surface-wave measurements, such as the ambient-noise technique, as well as array-based tomographic imaging methods have found increased popularity. The Eikonal tomography method, so termed by Lin et al. (2009) because of its relation to the Eikonal equation (e.g., Wielandt 1993), relies on dense array measurements and is based on the direct conversion of phase travel-times into phase-velocity maps without the need for an inversion. The method has been successfully applied to the USArray using surface wave measurements both from ambient noise and from earthquakes (e.g., Lin et al. 2009; Lin & Ritzwoller 2011a) but also on more local scales (e.g., de Ridder & Dellinger 2011; Mordret et al. 2013; Xu et al. 2016).

In the present study we make use of ambient-noise surface-wave measurements from the AlpArray experiment (Fig. 1, Hetényi et al. 2018) evaluated over two years (2016 – 2017). It has been shown in various regions that crustal anisotropy can be imaged with ambient-noise techniques (e.g., Lin et al. 2009; Fry et al. 2010; Lin & Ritzwoller 2011a; Gallego et al. 2011; Guo et al. 2017). The additional information contained in the azimuthal anisotropy can help to understand the tectonic evolution, because it is sensitive to preferential orientation of structures from the smallest (mineral alignment) to the largest scale (kilometer scale folds and faults, asthenospheric flow field) (e.g., Nicolas & Christensen 1987; Kern 1990; Silver 1996). This adds a dynamic component to the observations, linked to temporal variations such as the strain field.

The European Alps are a complex and relatively small mountain belt which was mainly formed by the continental collision of the European and Adriatic plate around 35 Ma ago (Fig. 1, Handy et al. 2010; Carminati et al. 2012, and references therein). The indentation of the Adriatic plate into the European one led to major crustal reorganizations such as a mantle wedge being pushed to crustal depths in the Ivrea zone (e.g., Malusà et al. 2015; Zhao et al. 2015) and, in the Neogene, to the sinistral movement along the Giudicarie fault and the exhumation of the Tauern window (e.g., Scharf

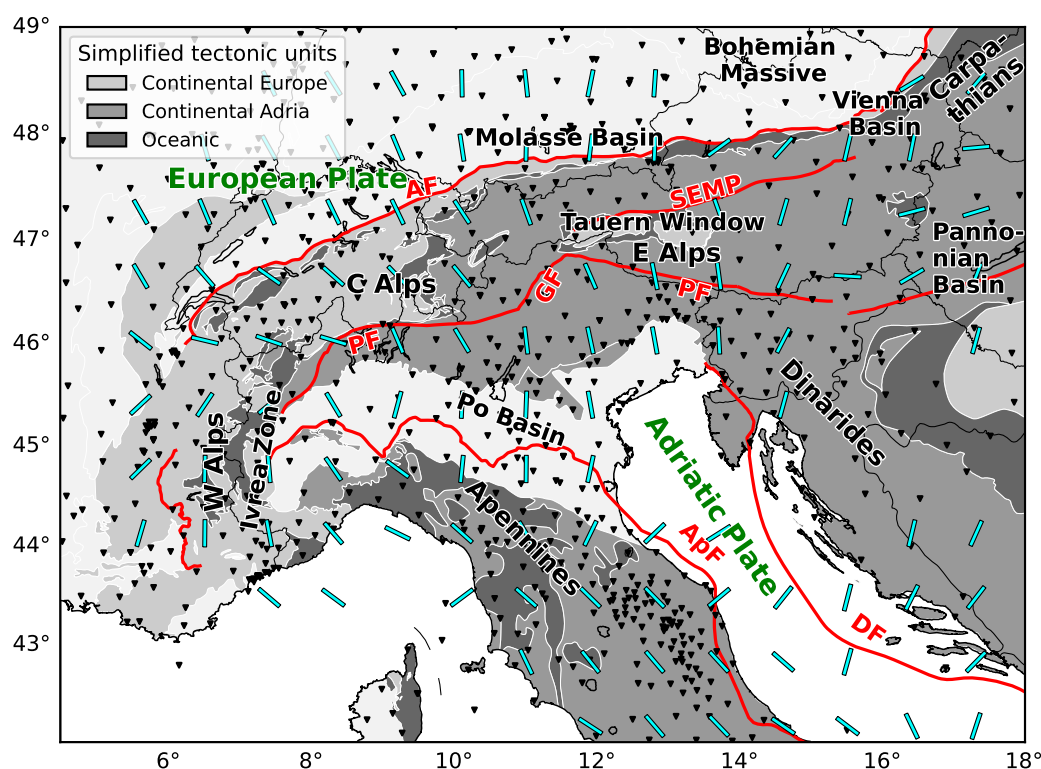


Figure 1. Tectonic overview map showing station locations (black triangles, permanent and temporary AlpAr-ray stations) and a simplified principal stress field (cyan, stress directions averaged in 100 km radius, dataset from Heidbach et al. 2016). AF Adriatic Front, ApF Apenninic Front, DF Dinaric Front, PF Periadriatic Fault, GF Giudicarie Fault, SEMP Salzach-Ennstal-Mariazell-Puchberg fault. Tectonic units and major lineaments simplified from Schmid et al. (2004, 2008); Handy et al. (2010).

et al. 2013; Verwater et al. 2021). The latter was supported by an eastward extrusion of the eastern Alpine units between the Periadriatic Fault in the South and the SEMP fault in the north (Scharf et al. 2013). This movement was likely triggered by the northeastward retreating subduction of the last remnants of the Tethys ocean during which the arcuate shape of the Carpathians was formed and the Pannonian basin opened (Handy et al. 2014, and references therein). The Carpathians are now almost entirely separated from the Alps by the Pannonian basin and the Vienna basin (Fig. 1). At the junction, the Carpathians bend northeastward around the Bohemian Massif, an area of thick and old continental crust that was amalgamated during the Variscan orogeny (e.g., Schulmann & Gayer 2000; Franke et al. 2017). These major changes, first from the continental plate collision and later the large reorganizations at the beginning of the Neogene, severely affected both crustal and mantle structure in the Alpine region. For example, slab break-offs have been proposed at different times and for different parts of the Alps (for a review see Kstle et al. 2020). Indications for a slab break-off under the eastern Alps have been found by Qorbani et al. (2015) when evaluating the azimuthal anisotropy from SKS

splitting data. The pattern of crustal seismicity in the central Alps has been explained with buoyant crustal material that was dragged down by the retreating European slab (Kissling & Schlunegger 2018). Such a process is expected to affect the strain field in the Alps and thus leave an imprint in the crustal anisotropy. Currently, there are, however, hardly any studies that image the anisotropic structure in the Alps at sufficiently high resolution to provide an understanding of how anisotropy links to past and ongoing tectonic processes (Fry et al. 2010; Alder et al. 2021). With this work we will thus present and discuss Eikonal tomography as a potential method to image azimuthal anisotropy at crustal and uppermost mantle level from surface waves. In the following we will continue previous efforts (Kstle et al. 2016) to provide an automated and robust phase-velocity picking algorithm from ambient-noise based Love- and Rayleigh wave cross-correlation measurements. The phase-velocity curves are then used to create azimuthally anisotropic maps of the phase-velocity structure by applying the Eikonal tomography method. The potential but also the limits of the method that can lead to a significant bias in the amplitudes of the inferred anisotropic field will be discussed. Both methods (phase-velocity picking and Eikonal tomography) are made available as Python based tools that are free to use, easy to modify and run platform independent on any machine (supplement).

2 METHODS

2.1 Data preparation and cross-correlation calculation

In this study, we use two years of continuous data recorded at all available AlpArray seismic network stations (permanent and temporary). The data processing is handled with a slightly modified version of the ANTS 2 toolbox (link in acknowledgements), which includes the following steps: (1) Removal of time windows after large earthquakes ($MW > 5.6$), for which the earthquake information is taken from the GCMT catalog (Dziewonski et al. 1981; Ekstrm et al. 2012). The length of the time window to be removed from the record is chosen according to the approximation by Ekstrm (2001). (2) Local earthquake events are requested via the IRIS catalog (www.iris.edu) and a time window, a few seconds before the estimated first P-wave arrival until all direct signals traveling with velocities 1 km/s have passed, is removed. (3) Seismic signals from events that do not appear in the used catalogs and other high-energy sources are removed, applying a filter that compares the signal standard deviation of subsequent time windows according to Boue et al. (2013). (4) Cosine tapering, detrending and demeaning of all data. Each window has a maximum length of one day. (5) Antialias (lowpass) filter with a cutoff frequency at 1 Hz. (6) Downsampling to 2 Hz. (7) Removal of the instrument response with a waterlevel deconvolution, including a pre-filter (flat between 2 – 200 s, cutoff periods at 333 s and 1 s).

From the pre-processed data, cross correlations are calculated between the vertical records (ZZ) of all available stations pairs. Stations pairs with an inter-station distance smaller than 20 km are skipped. The data is cut into windows of 1 hr, with successive windows having an overlap of 60%, each window is cosine tapered (2.5% at the beginning and end of each window) and linear trends are removed. We then apply a Fourier transformation and whiten the signals in the frequency domain by division with the absolute of the spectrum plus a waterlevel for stabilization. From the whitened spectra, the daily cross correlations are calculated and stacked resulting in a total number of 261,388 vertical-component correlations.

2.2 Phase-velocity extraction

From the cross correlations, phase velocities between station pairs are determined by using the zero crossings of the cross-correlation spectra (Aki 1957; Ekström et al. 2009; Kistler et al. 2016). The method is based on the assumption of a 2D wavefield (e.g., surface waves) composed of plane waves traveling in random directions. If this wavefield is recorded for a sufficiently long time at two stations, cut into windows, correlated and stacked, the resulting cross-correlation spectrum will resemble a Bessel function (Aki 1957). The argument of the Bessel function depends on the inter-station distance times frequency divided by phase velocity, thus, for a given set of these parameters, its zero crossings are known. The phase velocity can therefore be determined from a cross-correlation spectrum by fitting its zero crossings to the ones of the Bessel function. This approach does not rely on the amplitude information of the cross-correlation spectrum which is normally distorted by the variability of energy arriving for different frequencies and by applying the spectral whitening. The cross-correlation spectrum is often affected by noise, inhomogeneous microseismic source distributions and very low energy at the low-frequency end of the spectrum. Consequently, zero crossings may be missed or double crossings appear and it becomes impossible to fit a unique Bessel function to a given spectrum. The non-uniqueness can be partially resolved by restricting the range of allowed phase velocities to realistic values. In the case of Rayleigh-wave phase velocities, extracted from the ZZ cross correlations, we only allow values between 1.5 – 5.0 km/s which represent the range of expected phase-velocities for these waves at our periods of interest (2 – 200 s). The procedure is illustrated in Figure 2 and consists of the following steps: (1) Cross correlations for which less than 150 days are stacked are discarded; (2) applying a time domain filter that suppresses signals arriving with a velocity below 1 km/s and above 5 km/s. This results in a smoothed spectrum in the frequency domain; (3) the signals at positive time lags and negative time lags are treated separately and if the picked phase velocities for the two arrivals are too different (mean difference >0.3 km/s), the whole cross correlation is dis-

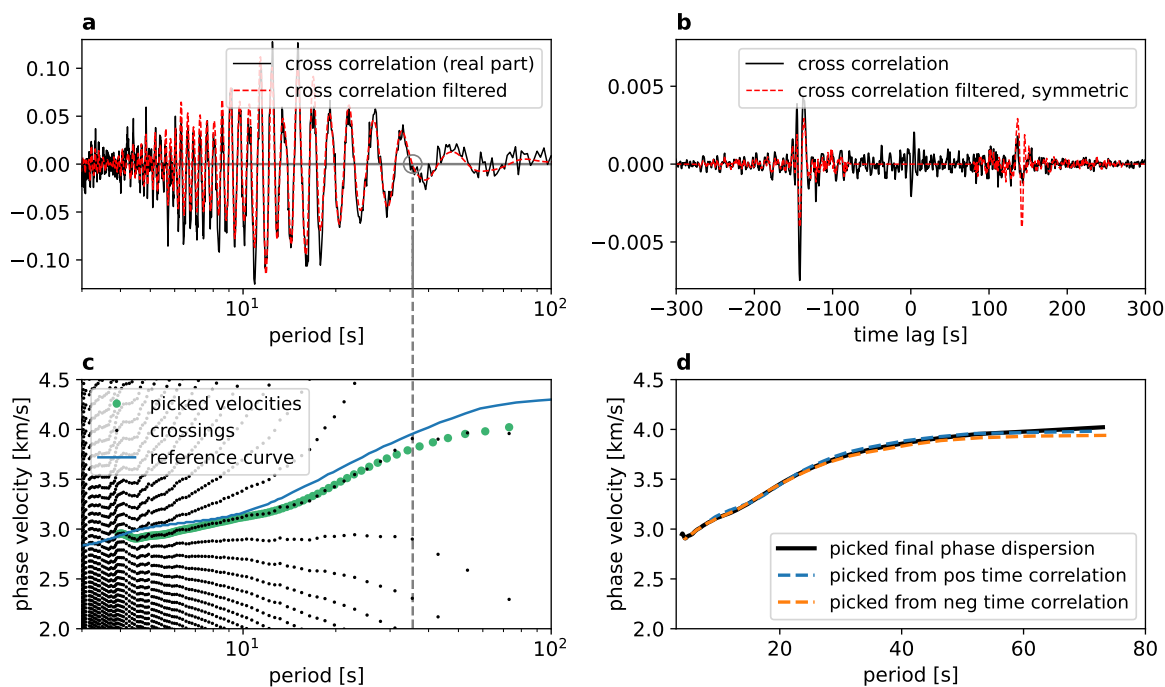


Figure 2. Example of the zero-crossing picking method for the station pair OX.FUSE, Z3.A073A, at an inter-station distance of 398 km. Panels **a** and **b** show the vertical component cross correlation in the frequency and in the time domain. The red dashed lines illustrate the effect of the velocity filter between 1 – 5 km/s. The time domain cross correlation is further symmetrized by discarding the imaginary part of the cross-correlation spectrum. The resulting phase-velocity curve is shown in the bottom panel. **c** shows the phase velocities associated to the zero crossings, exemplarily illustrated by the gray dashed line between panels **a** and **c**. **d** shows the good fit of the dispersion curves when only the cross correlation at positive/negative lag times or the symmetric (final) one is used.

carded (eliminates $\sim 20\%$ of the available data); (4) otherwise, the correlation is symmetrized and a final phase-velocity dispersion curve is picked.

The picking procedure itself is similar to the one described in Kästle et al. (2016). Each zero crossing in Figure 2 can be associated with multiple phase velocities as illustrated in Figure 3. To resolve this ambiguity between parallel branches, a reference curve, for example, derived from a regional average velocity model, is necessary that guides the picking algorithm at the low-frequency end of the spectrum. For low frequencies, the branches are sufficiently far apart, so that a unique pick can be taken. The original procedure of Kästle et al. (2016) is modified such that the phase velocities are not picked directly from the zero crossings as this may result in rough dispersion curves or wrong picks in case of noisy data. Instead, an elliptical-shaped area around each zero crossing is defined and an intensity is assigned within this area, ranging from 1, at the location of the zero crossing, to 0, at the boundary of the ellipse (Fig. 3). By summing the overlapping contributions from all ellipses, a smooth

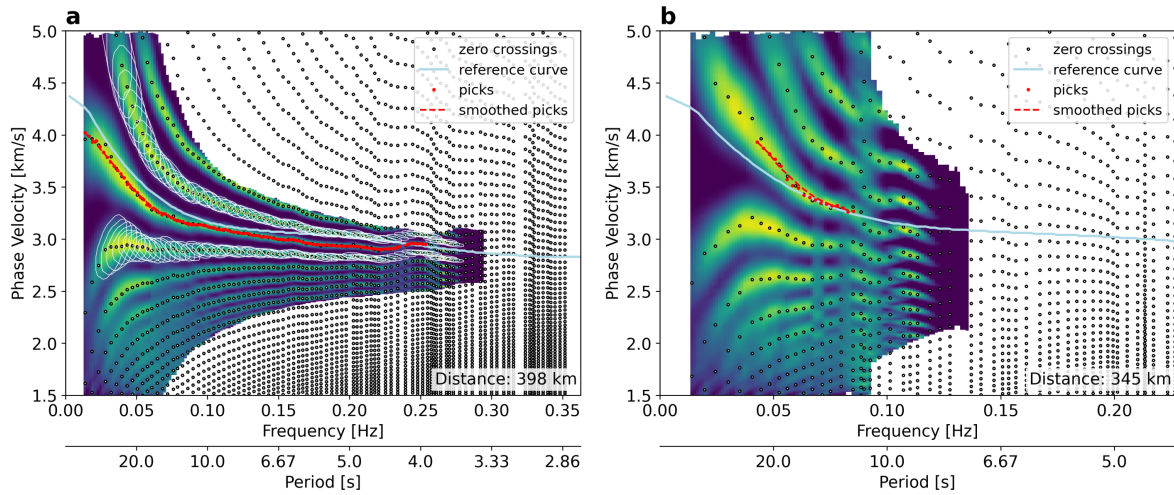


Figure 3. Procedure to extract phase velocities from the zero crossings of the cross correlation spectra. For each zero crossing, a multitude of Bessel functions can be found that pass through it, resulting in the ambiguity of the sub-parallel branches. The correct branch is chosen by starting the picking procedure close to the reference curve, at the low-frequency end. The algorithm stops automatically when the data quality is too bad to choose a good next pick. The background colors scale with the number of nearby zero crossings and are controlled by the white ellipses around each zero crossing. For better visual clarity, only the ellipses along two branches are shown in panel **a**. The zero crossings in panel **a** are from the cross correlation in Figure 2 (OX.FUSE, Z3.A073A). Panel **b** shows the same for a station pair with lower data quality (SK.MODS, Z3.A359A). At the low frequency end, the branches are too far from the chosen reference curve so that the choice of the right branch is ambiguous. The picking algorithm starts thus at higher frequencies. Because of jumps in the crossings, the picking is not completed and the result discarded.

intensity field is created and picks are taken where the intensity is maximized. This can be understood as a Kernel Density Estimation (KDE) with a cosine shaped kernel varying between 1 in the center and 0 at the edge of the ellipse. Size and orientation of the kernels/ellipses have to be chosen carefully, as the x- and y-axis have very different values and as the branches become narrower with increasing frequency. We deal with this issue by making an estimate of the y-axis distance between branches and the x-axis spacing between subsequent zero crossings. The estimate is based on the reference curve and on previous picks, which also controls the orientation of the elongated axis of the ellipses. Our implementation allows to easily adjust the picking behavior by modifying the kernel sizes depending on the application and data quality. The full code is available online and in the supplement to this article. With the applied criteria, we obtain a total of 164,116 phase-velocity curves from ZZ correlations. The described program can also extract phase velocities for the horizontal component correlations (TT, RR), in this case the second order Bessel function term is taken into account as discussed in Kstle et al. (2016).

2.3 Isotropic Eikonal tomography

The procedure described in the following is available as a Python tool from the supplementary material to this article. We adapted this tool from previous works of Lin et al. (2009) and Lu (2019). The Eikonal tomography method was originally proposed by Lin et al. (2009) and is based on the Eikonal equation (e.g., Shearer 2009),

$$\frac{1}{c^2} = |\nabla T|^2, \quad (1)$$

which relates the phase velocity c to the gradient of the travel-time field ∇T , valid at the high-frequency limit. Lin et al. (2009) argue that the method takes ray bending into account and, despite the high-frequency assumption, approximates the influence of the finite-frequency kernel. It has been shown for ambient-noise applications that the typical error introduced by this high-frequency approximation is below 2% of the mapped velocity variations (Lin & Ritzwoller 2011a; Mordret et al. 2013). The application of this method is straightforward, the travel times from one arbitrarily chosen central station to all other stations are interpolated onto a regular grid. By taking the inverse of the gradient of this travel-time field, the distribution of velocities is obtained (Eq. 1, Fig. 4). This procedure is repeated for all possible central stations. The final, isotropic map is calculated from the average of the ensemble of maps. In general, the method requires no regularization, compared to well-established linearized inversion approaches that apply damping or smoothing (e.g., Boschi & Dziewonski 1999). However, the method of interpolating the travel times from the single station measurements to a regular grid can have an important influence on the result. Small errors in the travel times can lead to strong variations in the gradient field which, by taking the inverse of these spurious gradients, may cause large velocity jumps. It is therefore necessary to apply an interpolation scheme that produces sufficiently smooth travel-time fields, to compensate measurement errors, without oversmoothing and thus losing information. In practice, previous works (Lin et al. 2009; Lin & Ritzwoller 2011a; Mordret et al. 2013) have often applied the spline-in-tension method (Smith & Wessel 1990). However, we prefer to use (smooth) radial basis splines (a comparison of four different interpolation schemes is shown in supplementary Figure S2). For the spline-in-tension method, the interpolated surface is required to pass through all nodal points (i.e. stations where a travel time has been measured), while the tension parameter can suppress spurious oscillations between points (Smith & Wessel 1990). With the use of smooth radial basis splines, we have the additional option to obtain a smooth surface without the necessity to fit all nodal points which can be advantageous in the case of measurement errors. Our tests indicate that the difference from the chosen interpolation method is relatively small at most periods, if spurious velocity spikes are removed (step (iv) below) before all models are stacked (Fig. S2). To be as independent as possible of user-defined regularization parameters, the smoothing parameter for

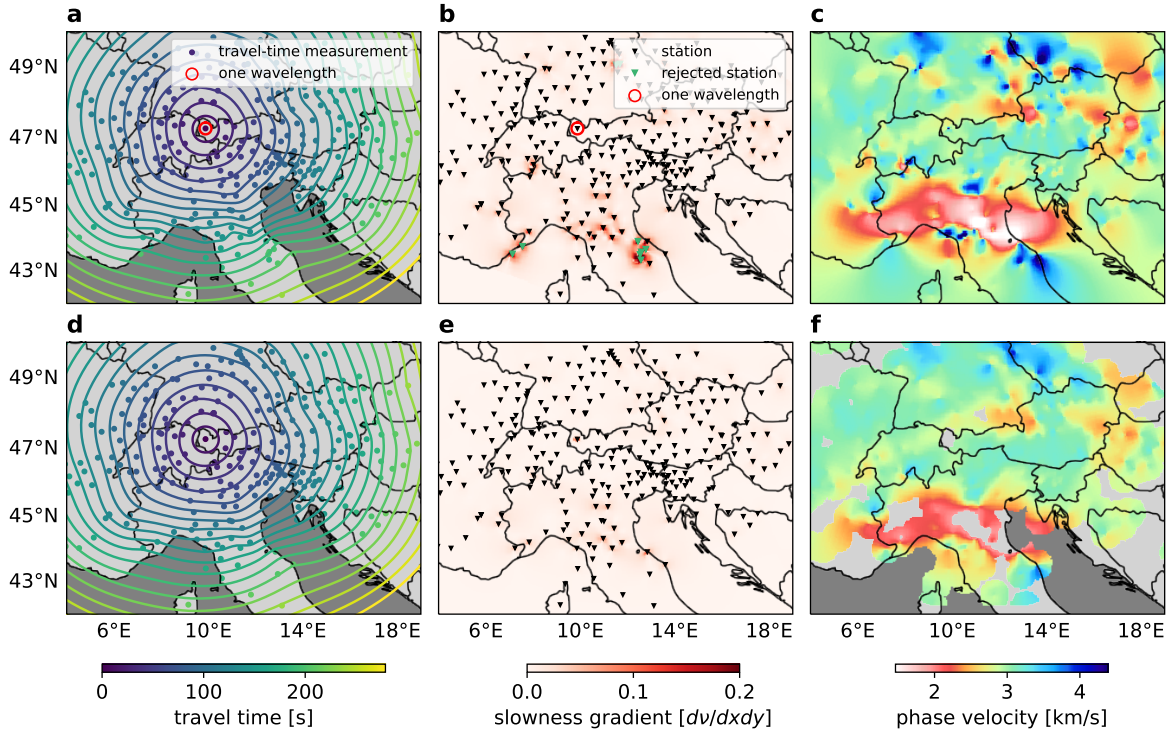


Figure 4. Example of the Eikonal tomography procedure for a single central station for data measured at a period of 6.5 s. Panels **a–c** show phase travel-time measurements, interpolated travel-time field, curvature of the travel-time field and the deduced phase velocities, all before any data rejection or interpolation smoothing has been applied. Panels **d–f** show the same after processing. The final phase-velocity map is created by taking the processed maps **f** and stacking them for all available central stations. Gray parts of the map indicate that measurements in these areas have been rejected, because the closest station is too far away, the azimuthal coverage is bad or there are too few values to obtain a stable average velocity estimate.

the interpolation is only controlled by the obtained velocities. The user has thus to define a threshold given in terms of deviation from the mean velocity, which is more intuitive and related to a physical property of the medium. The procedure is illustrated in Figure 4 and consists of the following steps:

(i) A central station is chosen and all phase-travel-time measurements between this station and all other stations are extracted from the dataset. Measurements from stations that are closer than one wavelength from the central station are ignored. We set a minimum threshold of 10 measurements.

(ii) An initial interpolation where the travel-time surface passes through all nodal points reveals areas of strong curvature. Travel-time measurements at stations that are associated with a curvature that deviates by more than a threshold of two standard deviations from the mean are considered outliers and are discarded. This rejects about 5% of the measurements.

(iii) The smoothing parameter of the interpolation starts at zero (no smoothing) is iteratively in-

creased until all velocities are below a user-defined threshold (in this work, three times the regional average velocity). If the interpolation grid is finer, it will automatically lead to a larger smoothing parameter, as a rough grid causes implicit smoothing by taking the blockmean of all station measurements within one grid cell.

(iv) Regions of the velocity map that show velocities that deviate by more than a second threshold (in this work, 50%) from the average velocity are removed from the map. This removes on average less than 1% of the mapped area.

(v) Regions of the velocity map that are outside the convex hull defined by the station locations, as well as regions that are too far away from the next station are removed. We choose a distance limit of 50 km at short periods, and one wavelength at long periods.

(vi) Steps 1 – 5 are repeated for all available central stations.

(vii) At all grid points, the mean and the standard deviation of the phase-velocities is calculated. Velocities that deviate by more than two standard deviations from the mean are rejected.

(viii) The final phase-velocity map is obtained by splitting the mapped phase velocities into azimuthal bins and taking the mean of the phase velocities in each bin. Areas where the gap in azimuthal coverage is greater than 60° and where less than 50 phase-velocity values are averaged are rejected. Secondly, the contributions of all bins are averaged for each grid cell. This two-step averaging procedure makes sure that the average is not biased by the number of measurements from different azimuths.

The example in Figure 4 shows how the procedure removes roughness in the travel-time field and very high amplitudes in the phase-velocity map. It is observable that the highest variance in the travel-time field appears at large distances from the central station, leading to spurious phase velocities. We checked that this is independent of the chosen interpolation method and interpret it as an effect of increasing measurement uncertainty with distance for the given dataset and also increasing distortions of the travel-time field by velocity variations within the medium. The effect is especially strong around the shown period of 10 s and decreases towards both shorter and longer periods. We also achieve good results for the Eikonal tomography method if we reject measurements that are further away than about 300 km from the central station. In this case, the interpolation smoothing becomes unnecessary (not shown here). However, because this leads to a rejection of a very large part of the dataset, we decide not to apply an upper distance limit.

2.4 Anisotropic Eikonal tomography

As shown by Lin et al. (2009), the Eikonal tomography method can be used to determine the azimuthally anisotropic velocity structure. For each central station, we can estimate not only the velocity

in each cell of the interpolated grid, but also the direction of the travel-time gradient, i.e. the direction of propagation. With this information it is possible to determine azimuthally dependent velocity variations by fitting them to the following equation for slightly anisotropic media (Smith & Dahlen 1973) to which we added a Ψ_1 term, similar to previous works Lin & Ritzwoller (2011a):

$$c(\omega, \psi) = c_0(\omega) (1 + A_1 \cos(\psi - \Psi_1) + A_2 \cos(2(\psi - \Psi_2)) + A_4 \cos(4(\psi - \Psi_4))), \quad (2)$$

where $c(\omega, \psi)$ is the phase velocity, depending on the angular frequency and the azimuth, c_0 is the isotropic velocity and A_1 , A_2 and A_4 are the amplitudes of the Ψ_1 , Ψ_2 and Ψ_4 components. In practice, values of A_x and Ψ_x are found by optimizing the least-square fit to the c values, identified as described above. The Ψ_1 term is non-physical, because it means that two waves propagating in opposite directions have not the same velocity which violates the reciprocity of the wave equation. However, Lin & Ritzwoller (2011b) have shown that the azimuthal velocity measurements can be biased in such way that there appears a Ψ_1 periodicity. Inclusion of the Ψ_1 term can thus avoid tradeoff with the Ψ_2 and Ψ_4 components and serve as an indicator for biased measurements (discussed below).

It can be difficult to get stable estimates of the anisotropy, because the expected amplitude of the azimuthal phase-velocity anisotropy is in the range of 0 – 3% (e.g., Fry et al. 2010) and therefore close to the expected range of measurement errors deduced from the mapped standard deviations and from previous works (1 – 2%, Kstle et al. 2016). Additionally, the sensitivity of the Eikonal tomography method to small travel-time errors can yield very large velocities at some locations and travel azimuths. It is therefore necessary to average over a larger area, which has already been shown in previous works (Lin et al. 2009; Lu 2019), while taking care not to lose too much information in regions where the fast axis direction shows strong lateral variations. After some testing, we found a good compromise by averaging over circular regions of 30 km radius and summarizing the azimuths of the velocity measurements into bins of 15°. The anisotropic parameters are only determined at locations where the total azimuthal coverage is more than 300°. In each cell, the isotropic phase-velocity is subtracted before performing the regional averaging and fitting procedure to minimize trade-off effects between isotropic velocity variations within the circular region and the anisotropic parameters.

3 SYNTHETIC EXAMPLE

We set up a test model as shown in Figure 5 and calculate synthetic travel-time data using the Fast Marching Method (FMM) so that the rays are bent according to the the velocity structure. The isotropic model is based on a satellite image which serves as approximation to a characteristic earth structure with different anomaly sizes and shapes. For this example, we use the same path coverage as in the

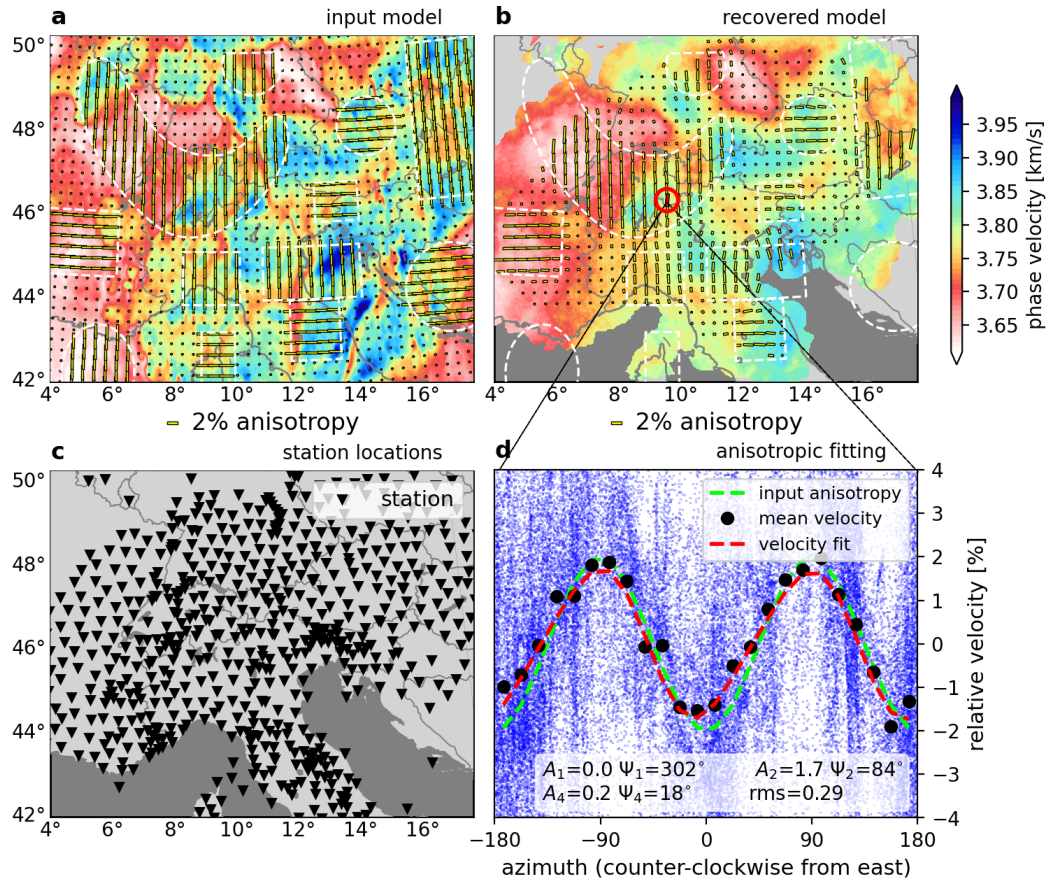


Figure 5. Synthetic test for an isotropic model (transformed from satellite image, credit: ESA, CC BY-SA 3.0 IGO) overlain by patches of either N-S oriented, E-W oriented anisotropy (2%) indicated by yellow bars. The data coverage is identical to that of the real dataset at 6.5 s period with the station configuration shown in **c**. **a** shows the synthetic input model, **b** the recovered model. The red circle indicates exemplarily the 30 km averaging radius for the determination of the anisotropic parameters. The red bar highlights one example location for which the fit to the anisotropic parameters is shown in **d**. The blue dots in the background give the individual measurements within the 30 km averaging radius.

measured dataset comprising $\sim 71,000$ measurements between station pairs resulting in phase-velocity models from 656 different central stations. An error is added to the synthetic data, defined in terms of velocity with a standard deviation of 0.02 km/s, which corresponds to a relative velocity error of 0.5%. This means that the absolute travel-time errors are larger for large inter-station distances, as is expected from the attenuation and the subsequently lower signal-to-noise ratio over large distances. The same processing steps and parameters as listed above are used to recover the model. The smoothing parameters in the interpolation was always zero as the velocity error never exceeded the threshold for the synthetic measurements (step (iii) in sec. *Isotropic Eikonal tomography*).

The large scale features of the example model are well recovered, smaller features are smoothed out leading to a general reduction of the anomaly strength, especially for smaller structures. Structures of sizes below about 30 km are not being recovered. The smoothing is caused by two related factors: (1) the travel-time field from each central station is only sampled at a subset of the stations shown in Figure 5c and is therefore missing details and (2) the incomplete reconstruction of the travel-time field causes errors in the velocity field (see blue dots Figure 5d) that lead to a smooth model when averaged over the models from all available central stations. The smoothing effect is also seen in the anisotropic parameters between patches of identically oriented anisotropy, as well as at the border of the patches.

In a next test, we check how stable the Eikonal tomography works in the presence strong velocity heterogeneities. We do so by increasing the amplitude of the isotropic velocity variation while keeping the anisotropic pattern identical to the one already shown in Figure 5. The resulting maps in Figure 6 show that the quality of the recovered isotropic model remains almost constant, illustrated by the stable relative errors (a relative residual of 10% for the 15%-anomaly model means an absolute error of 1.5%, i.e. 0.06 km/s). While the relative isotropic velocity residual does not change significantly with the anomaly strength, there is a clear dependence on the anisotropic residual. For the 5% model in Fig. 6, the anisotropic residual is relatively small and is visible mostly inside the patch regions with the same orientation as the input anisotropic direction. This indicates that the recovered anisotropy points in the right direction but has a smaller amplitude than the one in the input model. The residual tends to be larger for small patches and close to the model boundaries. An additional smoothing effect in the anisotropic structure can be explained by the fact that our approach averages measurements inside circular regions of 30 km radius for the determination of the anisotropic parameters. For higher isotropic anomalies (15 – 25%), the anisotropic fast axis orientation is still mostly correct within the patches, but a spurious signal appears outside these regions. It becomes clear that strong isotropic velocity variations introduce a bias in the anisotropic model.

3.1 Anisotropic bias

To better understand the source of this anisotropic bias and how it would affect the results for the Alpine models, a synthetic test with a purely isotropic velocity model, taken from the real-data models (shown below) is implemented (Fig. 7). The velocities in this example vary by -30% to +16% from the mean velocity. The very slow velocities are related to the thick sedimentary basin in the Italian Po plain. The synthetic travel times are modeled with a finite difference solver (Devito; Luporini et al. 2018; Louboutin et al. 2019) using a source wavelet with a dominant period of 6.5 s so that we can include finite frequency effects and reflections. The phase travel-time is measured in the frequency

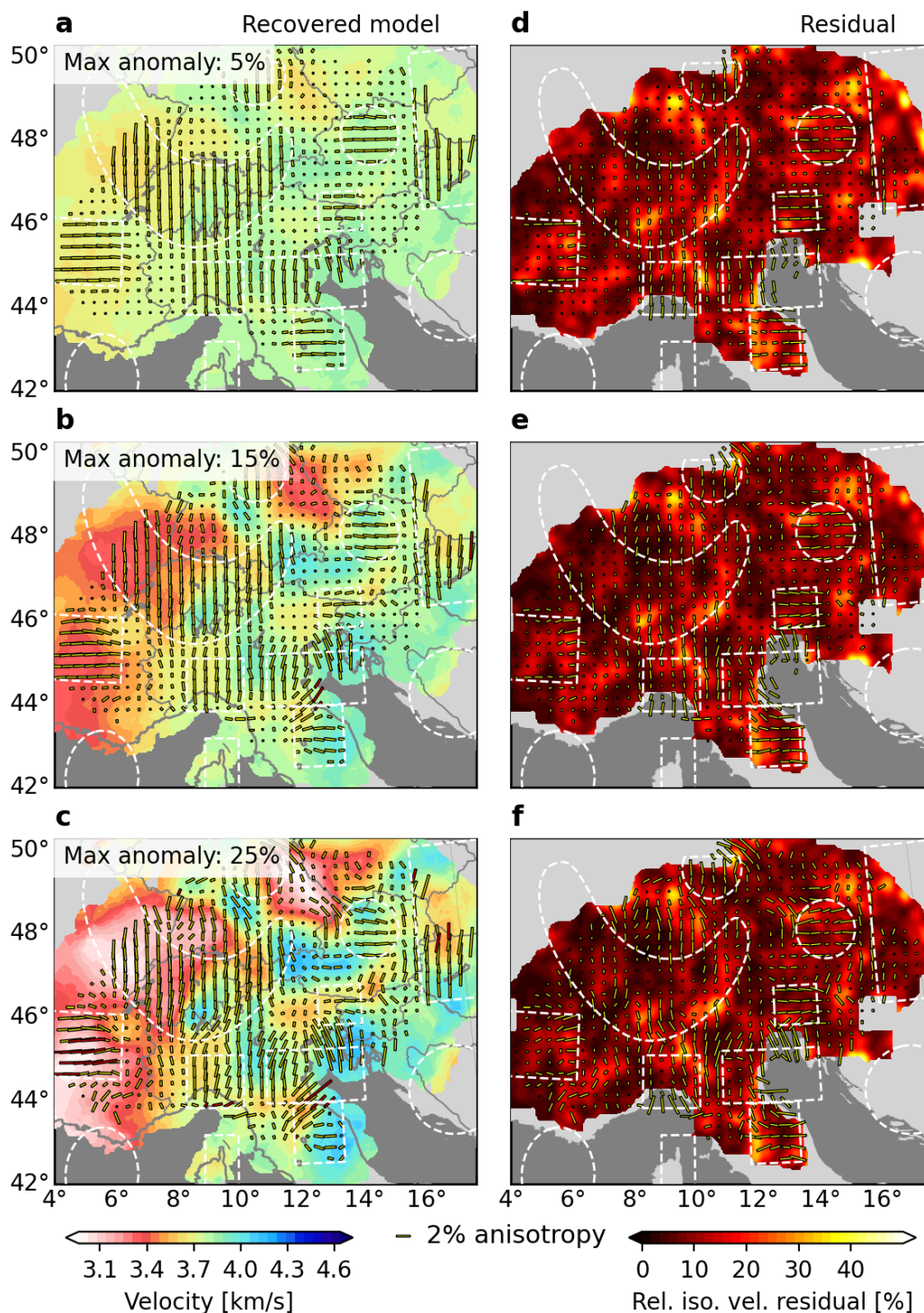


Figure 6. Synthetic tests to illustrate the effect of strong isotropic velocity heterogeneities. The input model for these tests is the same as shown in Figure 5a, however, the maximum isotropic velocity anomaly varies from $\pm 5\%$ (a, identical to Fig. 5) over $\pm 15\%$ (b) to $\pm 25\%$ (c). The strength and pattern of the anisotropy is identical between tests. Panels d–f give the isotropic velocity difference as color image and anisotropic residual calculated as vector difference. The isotropic residual maps are slightly smoothed for visual clarity. White dashed lines indicate the location of the anisotropic regions in the input model (Fig. 5).

domain from the phase of the cross-correlation function between source signal and the signal at the receiver locations. The recovered, final model in Figure 7b shows strong, spurious anisotropy with amplitudes of more than 5%. The areas where the anisotropic bias is most prominent coincide with areas where the travel-time field is strongly curved and concave shaped. In this example, no error is added to the data and the data coverage is idealized with all recorders active for all possible central stations (station locations in Fig. 5c). No data rejection based on local strong velocity variations, as we did in Figure 6, is performed: in the previous tests, the areas in the seas and close to the model boundaries were rejected because of bad station and bad azimuthal coverage. The spurious anisotropy seems to be less pronounced when the azimuthal coverage is good, but even in regions with perfect coverage (low velocity basin in southern Germany and directly north of the Po basin) the bias is still significant (2 – 3%).

The phase-velocity map for the single-central-station example in Figure 7c shows that there are significant errors in the recovered velocities, most prominent behind low-velocity zones. One reason for these artifacts is the occurrence of a secondary wavefront downstream from the sedimentary basins (Feng & Ritzwoller 2017). The first wavefront results from the signals traveling around the low-velocity area deforming it to a concave shape. The second wavefront is caused by the slower propagation velocity inside the basin. The basin itself acts like a lens that focuses the waves, therefore it is possible that the secondary wave package may have a higher amplitude. Typically, first and secondary waves are not clearly separated in time and will thus interfere (Fig. S4). The effects of slow sedimentary basins on wave propagation angles and amplitudes is discussed in detail in Feng & Ritzwoller (2017). Another effect is caused by back scattering which leads to an undulating phase error (and consequently velocity error) with a $\lambda/2$ periodicity (i.e. wavelength $\lambda \approx 20$ km at period 6.5 s) as described in Bodin & Maupin (2008); Lehujeur & Chevrot (2020). The station sampling distance in Figure 7 is larger than this periodicity, thus making it hardly visible, but the effect can be seen at longer periods and for very dense sampling examples (Figs. S5–S9).

Lin & Ritzwoller (2011b) study in detail the bias in anisotropy from inhomogeneous media when applying Eikonal tomography to data from the USArray. The typical station spacing is ~ 70 km in USArray and ~ 50 km in AlpArray which gives a comparable setup for testing. They mainly attribute the bias to finite frequency effects causing backwards scattering in the vicinity of the receiver locations (mostly responsible for a bias in the Ψ_1 anisotropy) and to wavefront healing (Nolet & Dahlen 2000) due to the large size of the sensitivity kernels (responsible for a bias in the Ψ_2 anisotropy). Both Bodin & Maupin (2008) and Lin & Ritzwoller (2011b) find that the bias becomes stronger with increasing velocity contrast, as is the case in our study.

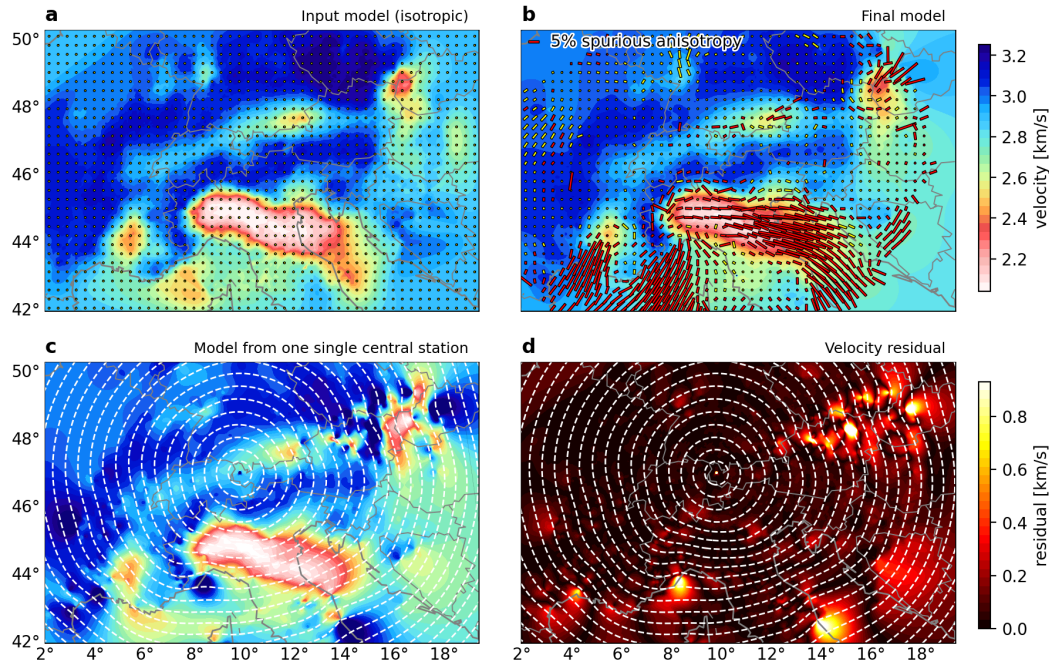


Figure 7. Synthetic test with input model taken from the real data model at 6.5 s. The dominant period for the source signal is chosen accordingly. For the single station example in **c**, the same central station as in Fig. 4 is used. In this idealized example, the travel time field is recorded at all station locations that are shown in Fig. 5c. The final model in **b** is derived from the ensemble average of all individual single-central-station models. The bars indicate the anisotropy. Red/yellow color of the bars indicate whether the standard deviation of A_2 (eq. 2) is above/below 0.5. The velocity residual in **d** gives the difference between the models in **c** and **a**. White dashed lines indicate the iso-contours of the travel-time field.

This class of errors from wave interference affect the phase-velocity measurements directly. It could be reduced by picking first (direct) arrival times in the time domain which would be valid for our synthetic test where the source is almost perfectly monochromatic (Fig. S4). Preliminary tests show that using only the first-arrival travel-time field can indeed reduce the mapped artifacts (Figs. S5–S9). Realistic applications, however, typically deal with dispersive waves and make use of a frequency domain approach to determine phase travel-times, as for example the FTAN or the Bessel function method described in the previous sections where the entire wave train is taken into account. More than that, if direct and scattered wave packages are too close it becomes difficult or even impossible to isolate the first arriving wave.

The errors related to finite-frequency effects in the recovered velocity field can be better understood in the context of the Eikonal equation (Eq. 1) that is only valid for smoothly varying media and approximately plane waves (e.g., Wielandt 1993). Equation 1 is a simplification, derived from a

Helmholtz representation of the wave equation, in which the amplitude term has been neglected. The full equation reads (Wielandt 1993):

$$\frac{1}{c^2} = |\nabla T|^2 - \frac{\nabla^2 A}{\omega^2 A}, \quad \nabla^2 = \frac{\partial^2}{\partial x^2} + \frac{\partial^2}{\partial y^2}, \quad (3)$$

where A is the amplitude of the wavefield. In terms of Wielandt (1993), the application of the Eikonal equation leads to the dynamic phase velocity, not the medium phase velocity which can only be obtained when the amplitude distribution is taken into account (even then an error remains as shown by Friederich et al. 2000). The curvature of the wavefield from the point source in Fig. 7 causes only a relatively low error (< 0.1 km/s), but other effects such as wave focusing in low-velocity zones have a more severe influence (Figs. S5–S9). The influence of the amplitude term has been studied in several previous works (Bodin & Maupin 2008; Lin et al. 2009; Lin & Ritzwoller 2011a; Lehujeur & Chevrot 2020) and it has been proposed that it becomes negligible at short periods (increasing ω in Eq. 3), for example, below 1 s for the local dataset of Mordret et al. (2013) or below 40 s for the western part of the USArray data in the work of Lin & Ritzwoller (2011a). Our tests confirm that at long periods much larger portions of the map are biased if the amplitude correction is omitted (for a long period example see supplementary Fig. S8–S9). Specifically, the $\lambda/2$ -periodic phase bias is strongly period-dependent and becomes larger at long periods.

Our tests indicate, however, that also in the short-period (6.5 s) finite difference simulation (finite frequency) and the FMM simulation (infinite frequency) a significant bias in the Ψ_2 anisotropy appears. In both cases, effects such as wave-front healing should play only a minor or no role. At high frequencies, the observed bias is mainly controlled by the incomplete reconstruction of the travel-time field by only being able to sample it at the receiver locations. If the travel-time field is strongly distorted, as expected behind strong velocity heterogeneities, extremely dense sampling would be necessary to be able to properly recover it. Typically, this is not the case, resulting in a smoothed version of the travel-time field and thus a phase-velocity bias that is dependent on the azimuth of the wave propagation with respect to the location of the anomaly. The infinite frequency tests (FMM) in Figures S5–S8 show that in case of perfect sampling and if no finite-frequency effects appear the recovered phase-velocity field is almost identical to the input model, as expected. The only remaining artifacts appear in narrow stripes, where the size of the grid cells is larger than the curvature of the travel-time field, and thus the estimation of the travel-time gradient fails. For a stable gradient estimate, the wave-front has to be approximately plane in the area covered by the gridpoint and its four neighbor points used to calculate the gradient. To prove the important influence of the travel-time field sampling in the Eikonal tomography method, we have repeated the test shown in Figure 7 calculating synthetics with the FMM method, i.e. no finite-frequency effects such as back-scattering, secondary wave fronts,

etc. appear. The resulting anisotropic bias is, however, almost identical to the one shown in the finite-frequency simulation (Figs. 7, S10–S11). From this we conclude that at short periods, finite-frequency effects are indeed negligible as proposed by Lin & Ritzwoller (2011a) or Mordret et al. (2013), but the wavefield under-sampling becomes the dominant factor. *Short* periods are in this context to be understood as relative to the inter-station spacing and depending on the complexities of the travel-time field caused by the velocity heterogeneities. The bias from incomplete travel-time sampling can affect the Ψ_1 , Ψ_2 and Ψ_4 anisotropic components alike, it is therefore recommendable to model all of them to avoid for example wrong mapping of a spurious Ψ_1 component into the Ψ_2 anisotropy (Lin & Ritzwoller 2011b).

Different from the finite frequency effects that directly bias the measured phase-velocities between station pairs, and thus will affect also other tomographic methods, the issue of the incomplete travel-time field sampling is unique to the Eikonal tomography method. The bias from the undersampled travel-time field may be partially mitigated by choosing a different interpolation scheme, however, with the herein discussed methods, we did not note a significant difference.

3.2 Addressing the Ψ_2 bias

In the isotropic phase-velocity maps, most of the discussed bias cancels out by azimuthal averaging. This has been shown analytically for the finite-frequency effects by Lehujeur & Chevrot (2020) and is also suggested by our tests that show a relatively stable isotropic error with increasing velocity anomalies (Fig. 6). However, for the estimation of the azimuthal anisotropy, the contributions from different azimuthal directions need to be treated separately, thus a bias remains. Bodin & Maupin (2008) and Lin & Ritzwoller (2011a) already indicated that including the amplitude term from eq. 3 can significantly reduce the influence from the discussed finite-frequency effects which we confirm in our tests shown in Figures S5–S8. However, a bias will remain, since also the Helmholtz equation is only approximately valid for surface wave propagation in a laterally heterogeneous medium (Friederich et al. 2000; Lin & Ritzwoller 2011a). We will not discuss this option in detail, because we estimate it to be unfeasible for typical ambient-noise applications for two main reasons: amplitude measurements from ambient noise are difficult because of issues such as non-uniform source distribution or typical non-linear pre-processing steps that affect different station pairs and time windows differently (e.g., Fichtner et al. 2020). More important, however, is the issue of interpolating the strongly varying amplitude information from the station locations onto a dense, regular grid, necessary to calculate the Laplacian of the amplitude field (eq. 3). In our synthetic example at 6.5 s period, we observe an increase in the wavefield amplitude by a factor of 4 in a very narrow stripe that is caused by the interfering wavefields, refracted from the strong velocity contrasts in the model (Fig. S6). In our tests,

we are only able to record and properly correct for the amplitude effect if we have perfect sampling, i.e. an extremely dense distribution of stations with a sub-wavelength spacing which is unrealistic in most real applications at short periods. Otherwise, the amplitude field is smeared out or distorted and cannot be used to correct the dynamic phase velocity. Finally, the incomplete reconstruction of the travel-time field poses an even more important source of bias at short periods that cannot be addressed by the amplitude correction.

An alternative to correcting the velocity bias is removing measurements in the map where the travel-time field is strongly curved and thus violates the plane-wave assumptions made in Eikonal tomography method (e.g., Mordret et al. 2013). The mapped region rejected by this approach changes with different central stations and at short periods only small areas need to be removed thus making it necessary to remove only a few percent of the measurements and still being able to recover the entire region in the ensemble average. This approach works very well in our tests where we have a perfectly dense station distribution (not shown here for the sake of brevity). However, in the case of realistic station distributions, as shown for example in Fig. 7, the regions of highly curved travel-time become smoothed out and cannot be properly identified anymore thus making this approach ineffective.

Lin & Ritzwoller (2011b) propose that the presence of the nonphysical Ψ_1 anisotropy may be used as indication of the presence of a bias in Ψ_2 . In Figure 8 we check for a spatial correlation of the bias in with the the Ψ_1 intensity, as well as with the velocity gradient and the uncertainty in the Ψ_2 amplitudes (i.e. std A_2). We find that in all three cases the spatial correlation is weak such that it is not straightforward to filter out biased anisotropic measurements using these three parameters as proxy. The closest spatial correlation is found with the uncertainty in A_2 which we calculate from the covariance of the least-squares fitting procedure to eq. 2. We will reject measurements where the standard deviation of A_2 is greater than 0.5. This value is based on the synthetic test results presented in Figure 6 and 7b (see red bars). From the discussion here it is clear that the A_2 standard deviation is only a proxy but no guarantee that all biased anisotropic measurements are excluded. For example, not all of the spurious anisotropy shown in Figure 6 is also related to areas above the threshold of 0.5 which would get rejected by this approach.

4 RESULTS FOR THE ALPARRAY DATASET

We apply the Eikonal tomography method to the presented AlpArray dataset and extract azimuthally anisotropic maps at periods between 3 and 80 s (Fig. 9). We only show isotropic velocities in regions where we have enough values for the averaging procedure and with good azimuthal coverage (see list in sec. *Isotropic Eikonal tomography*), the remaining parts are greyed out. The same applies for the anisotropic parts of the map. We additionally use the uncertainty in the anisotropic intensity, A_2 ,

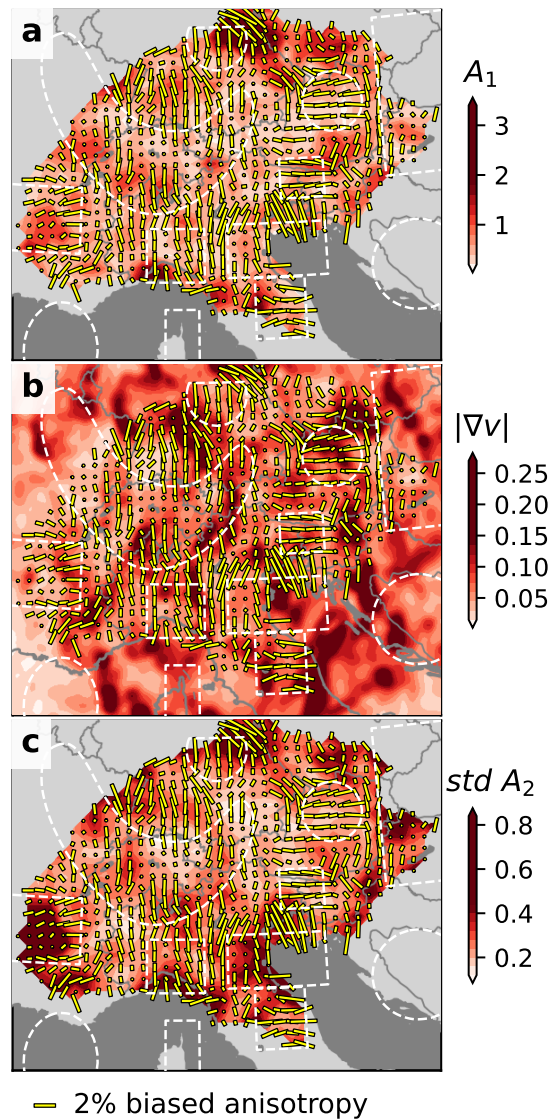


Figure 8. The anisotropic bias presented in Figure 6f ($\pm 25\%$ isotropic velocity variation) is compared to three different parameters: **a:** to the strength of the Ψ_1 anisotropy, **b:** to the gradient of the velocity field calculated from the input model and **c:** to the standard deviation of A_2 (amplitude of the Ψ_2 anisotropy; its standard deviation can be calculated from the fitting procedure to Eq. 2). A weak spatial correlation between the biased anisotropy and the strength of all three chosen parameters can be seen.

to identify regions where the anisotropic fast axes are likely biased. We show these measurements in grey as opposed to the remaining areas that are below this threshold, colored in yellow in Figure 9. The comparison of the potentially biased anisotropic areas of the maps with the results of the synthetic test in Figure 7 reveal that the anisotropic bias is mostly an issue in and around areas of very slow phase velocity. The anisotropic fast axes strengths and directions that are identified as biased follow a similar pattern as in the synthetic test: the fast axes align with the shape of the low velocity anomalies, parallel

to the elongation axis within the low velocity areas and curving around the edges, i.e. parallel to the boundary of the velocity contrast. The uncertainty in A_2 is lowest around 20 s period and increases both towards shorter and longer periods. However, the analysis of the A_2 standard deviation can only serve as a proxy for biases anisotropic measurements, there are also other factors that influence the uncertainty, such as errors in the measured phase travel-times. Some regions where the anisotropic fast axis is biased may not be identified at all as can be seen from the test in Figure 8.

For each map shown at a certain period, we give a depth range which we derive from the calculation of sensitivity kernels based on the model of (Kstle et al. 2018, Fig. S1). The min/max values of the depth ranges are chosen so that, on average, 50% of the surface under the sensitivity kernel lies within that range. Low velocity areas, such as the sedimentary cover in the Po-basin or the thick crustal root underneath the Alps, shifts the peak sensitivity to shallower depths. For example, in the map at 30 s in Figure 9, velocities and fast axis directions under the Alps and Apennines are most influenced by crustal structures, while outside, they are mostly influenced by mantle features. The isotropic structures are very similar to the ones obtained by other inversion approaches previously applied in the Alpine area (e.g., Kstle et al. 2018; Lu et al. 2018). The mapped velocities are smoother compared to these previous studies with slightly reduced anomaly amplitudes compared to a linearized inversion approach (Fig. S2). This observation is, however, strongly dependent on the chosen thresholds in the Eikonal tomography method (see sec. *Isotropic Eikonal tomography*) and the regularization parameters in the linearized inversion.

5 DISCUSSION

5.1 Variance reduction

The variance reduction serves as a measure to compare the final models data fit to the fit to a constant velocity model. We define it as

$$variance_{reduction} = 1 - \frac{\sum (t_i^{mod} - t_i^{obs})^2}{\sum (t_i^{ref} - t_i^{obs})^2}, \quad (4)$$

where t_i is the travel time between the i -th station pair in the observed data (*obs*), in the final phase-velocity maps (*mod*) and in the constant velocity reference model (*ref*). The variance reduction gets closer to 1 as the fit improves. The travel time in the final phase-velocity model is not a direct output of the Eikonal method. We approximate it calculating the travel time on a straight ray path between station pairs.

For the real data case, the variance reduction of the purely isotropic model is around 0.8 for short

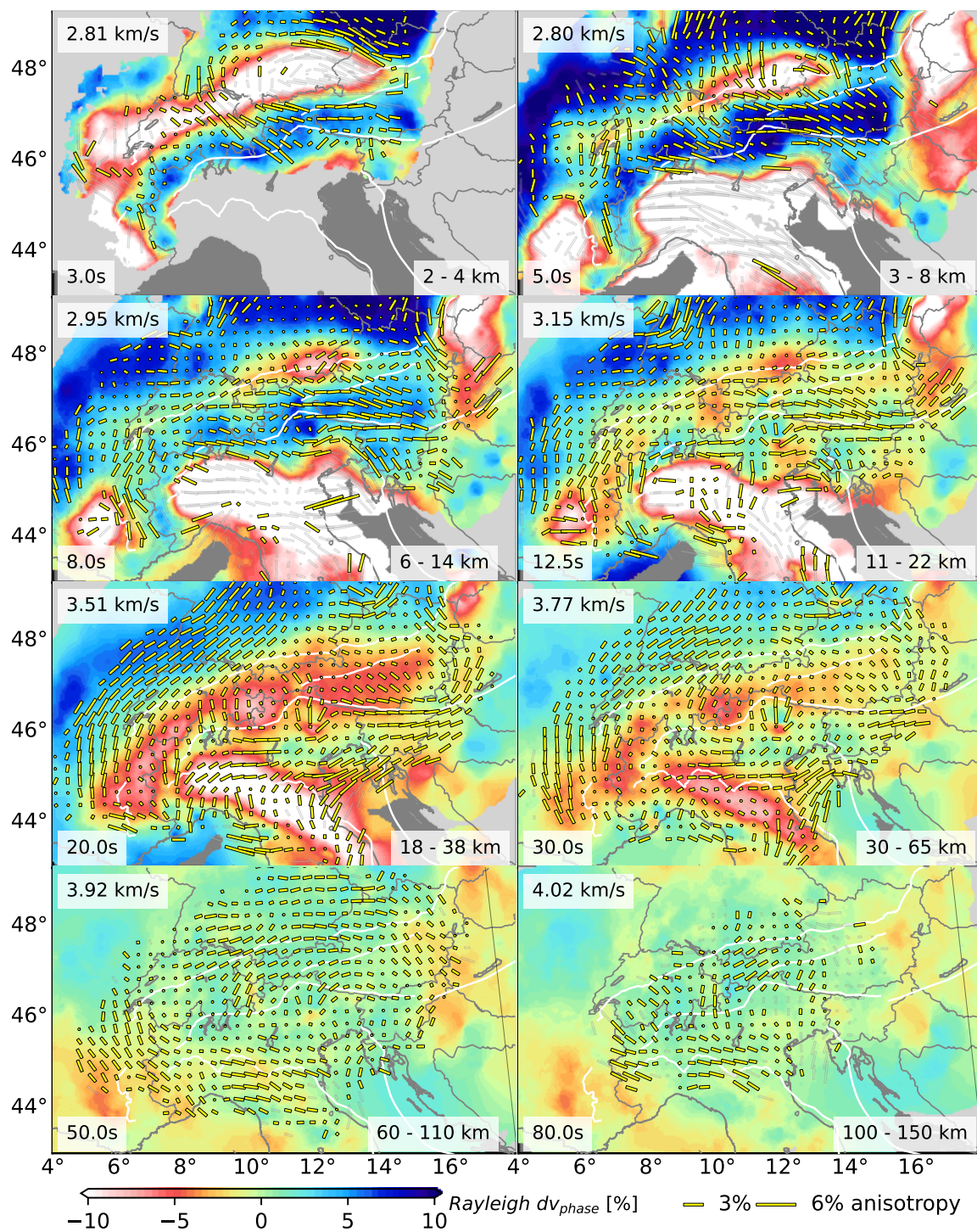


Figure 9. Rayleigh fundamental-mode phase-velocity maps at selected periods. Velocities are given as deviations from the mean velocity shown in the top left corner of each panel. Yellow bars indicate the direction and strength of the azimuthally anisotropic fast axis. Greyed out bars indicate that the standard deviation of A_2 exceeds 0.5. In regions where the majority of the bars are grey the anisotropic parameters are thus likely to be biased. White boundaries show tectonic limits and major faults from Schmid et al. (2004)

Table 1. Variance reduction and mean anisotropic amplitudes (percent) at different periods. The variance reduction values are calculated from eq. 4 using the real data results presented in Fig. 9 for the isotropic and anisotropic velocity variations. The variance reduction is always higher when the anisotropy is taken into account except at 50 s period. The anisotropic amplitudes represent an average over the entire mapped area based on the regression applied to eq. 2.

Period	isotropic	anisotropic	avg. A_1	avg. A_2	avg. A_4
3.0	0.758	0.793	1.25	1.40	0.96
5.0	0.734	0.764	1.77	1.70	0.90
8.0	0.831	0.843	1.32	1.15	0.72
12.5	0.778	0.791	0.91	0.99	0.56
20.0	0.836	0.856	0.67	0.98	0.37
30.0	0.533	0.558	0.70	0.79	0.44
50.0	0.057	0.052	0.74	0.69	0.54
80.0	0.013	0.021	0.84	0.76	0.76

periods up to 25 s (Tab. 1). At longer periods, it decreases to values close to zero (no improvement compared to the constant velocity model). This behavior is also observed with classical inversion approaches (Kstle et al. 2018) and has three main reasons: (1) the ray approximation used in this test which is not valid for the large wavelengths at longer periods; (2) the data quality decreases above 30 s for the presented ambient-noise measurements making it more difficult to get a good data fit; (3) the phase-velocity model at long periods shows only small velocity variations such that it is always closer to the constant velocity reference model. Including the anisotropy has only a small but positive effect on the variance reduction (~ 0.01), improving the data fit which we take as indication that the method is working. We note that, at periods below 30 s, the anisotropic variance reduction gives slightly improved values if we choose to average measurements in within a smaller radius, instead of the 30 km radius applied above.

The variance reduction in the synthetic example in Figure 6 gives similar values, with a slightly more pronounced effect from including the anisotropy (~ 0.03). Of course, there is no period dependence, as the synthetic data is calculated with the same error and same ray approximation for all periods.

5.2 Non-homogeneous noise source distribution and Ψ_4 anisotropy

Ambient-noise based travel-time measurements require a homogeneous distribution of noise sources from all azimuthal directions, otherwise the result may be biased (Yang & Ritzwoller 2008; Tsai 2009; Weaver et al. 2009; Yao & van der Hilst 2009; Kstle et al. 2016). We have noted earlier that even small errors in the travel-time field can lead locally to large phase-velocity variations and thus an increase in

uncertainty of the final phase-velocity maps. An inhomogeneous noise-source distribution would likely influence neighboring station measurements similarly and therefore only make a small contribution to the roughness in the travel-time field. Lin et al. (2013) similarly argue that the inhomogeneous noise source distribution plays a minor role for the Eikonal equation tomography, because the gradients are less influenced, compared to classical straight ray tomography. Also, averaging over the ensemble of phase-velocity maps will cancel out most of this bias. However, for the determination of the anisotropic parameters, the effect may have a negative effect on our final maps. Synthetic tests of Kästle et al. (2016) for a typical situation in the Alpine region indicate that the bias from non-homogeneous source distribution varies with a Ψ_4 periodicity with an amplitude of 0.5%. We therefore assume that the bias on the discussed Ψ_2 anisotropy is low compared to the observed anisotropic amplitudes. The observed amplitude of the Ψ_4 anisotropy is always about 30 – 50% smaller compared to the Ψ_2 anisotropy at periods up to 25 s (Tab. 1). At longer periods the difference approaches zero. Also in the synthetic example, the amplitudes of the Ψ_4 anisotropy are non-negligible and about 70% smaller than those of the Ψ_2 anisotropy. Our synthetic tests indicate that the spurious Ψ_4 anisotropy is not confined to the region of the anisotropic patches so that we can exclude a mapping of the Ψ_2 anisotropy into the Ψ_4 anisotropy. We can also exclude any bias from a non-homogeneous noise source distribution in the synthetic example. Thus, we infer that part of the Ψ_4 anisotropy is caused by errors in the reconstructed travel-time field, related to data errors and to the sparse sampling of the travel-time field.

5.3 Ψ_1 anisotropy

Tests for the herein presented dataset indicate that the Ψ_1 anisotropy appears at all periods and concentrates around certain areas such as the Ivrea zone in the western Alps, the sedimentary basins, and the borders of the mapped region (Fig. 10). The model-averaged amplitude of the Ψ_1 anisotropy is slightly smaller than that of the Ψ_2 anisotropy below 40 s and equal or larger above; the variation is small, however (Tab. 1). Lin & Ritzwoller (2011b) propose that a strong amplitude of the Ψ_1 anisotropy can be taken as proxy for a bias in Ψ_2 . They find in a synthetic test that the spurious Ψ_1 component is strongest at the border of low-velocity zones with their fast-axis pointing towards the fast velocity region. The same is true for the real-data example shown at 8 s period in Figure 10a. The synthetic tests of Lin & Ritzwoller (2011b) further show that the spurious Ψ_2 component, tends to be strongest inside the low-velocity regions, aligned with the major elongation axis of the low-velocity patches, similar to Figure 7b. We infer that this spurious Ψ_2 component leads to an increase in the A_2 standard deviation. This can be seen from Fig. 10e,f which exhibit both a strong Ψ_1 component but also a larger scatter in the mapped phase velocities, compared to the points in Fig. 10c,d. This justifies our choice of basing our rejection scheme in Figure 9 on the uncertainty in the amplitude of the Ψ_2 anisotropy

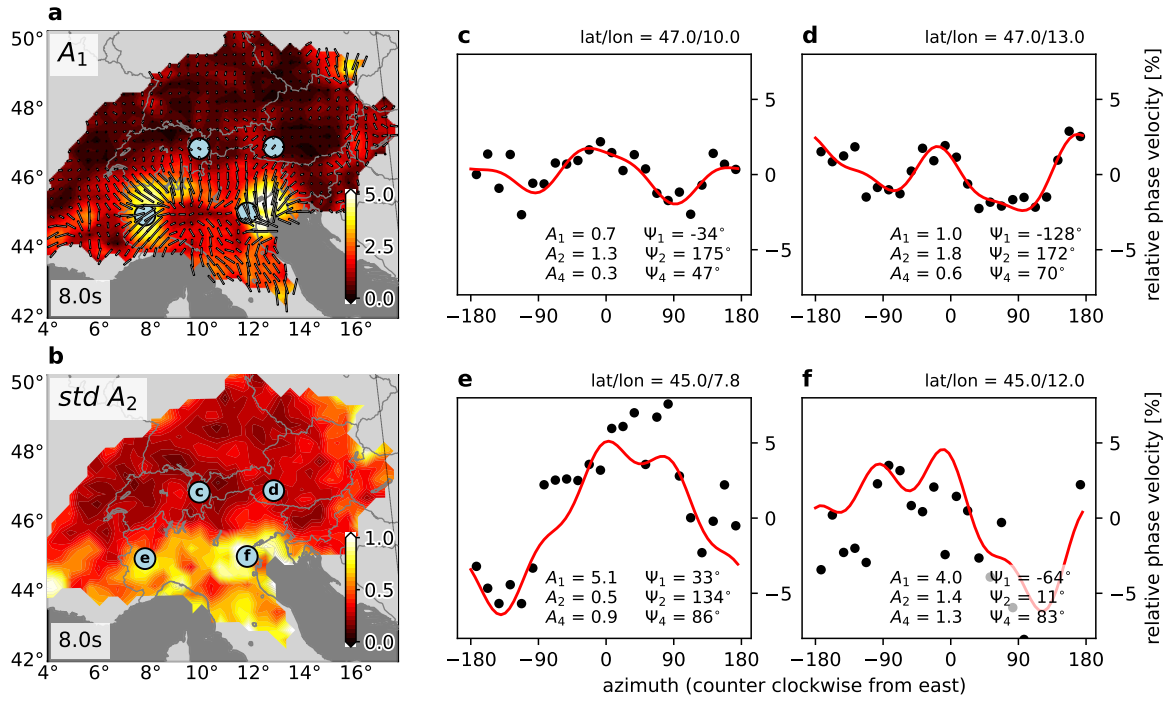


Figure 10. Azimuthal anisotropy at selected locations for the phase-velocity map at 8 s period. **a:** Amplitude of the Ψ_1 anisotropy and its direction. **b:** Standard deviation of A_2 . **c–f:** Mean velocities obtained in different azimuthal directions (black dots) and the regression fit (red line). The anisotropic parameters shown at the bottom of each panel correspond to those in eq. 2. The data for the panels **c–f** were taken from circular regions with 30 km radius as indicated in panels **a** and **b**.

which is spatially better correlated with the spurious Ψ_2 component. Different from Lin & Ritzwoller (2011b), we find that the Ψ_1 anisotropy is already pronounced at short periods (Fig. 10 at 8 s period). This may be due to the strong velocity contrasts from the sedimentary basins in our model area which did not play an important role in the studies of Lin & Ritzwoller (2011a,b) that only consider periods ≥ 40 s. It further indicates that the effect from under-sampling of the travel-time field has a similar influence on the mapped anisotropic bias (in Ψ_1 , Ψ_2 and Ψ_4) as from finite-frequency effects.

5.4 Sources of anisotropy

Different mechanisms can cause the azimuthal anisotropy in the crust and it is not easy to distinguish between these processes when interpreting the imaged structures. Laboratory experiments on rock samples show that at shallow depth, down to about 200 MPa (~ 5 km), the bulk anisotropy is dominated by microcracks (Kern 1990; Kern & Schmidt 1990). These (fluid filled) cracks are expected to be aligned perpendicular to the minimum stress direction and thus approximately parallel to the maximum horizontal stress and the anisotropic fast axis (Crampin 1994). An alignment of the fast axis is

also expected with structures such as rock foliation (Lschen et al. 1991), faults, folds or inclusions. All of these effects can be summarized as shape-preferred orientation (SPO) of the anisotropic fast axis. In contrast, the alignment of anisotropic crystals such as olivine (e.g., Nicolas & Christensen 1987), mainly in the mantle, or amphibole and biotite (Barruol & Mainprice 1993) which are also abundant in the lower crust, is classified as lattice-preferred orientation (LPO) and is the main source of anisotropy at greater depths. The named minerals show an alignment of their fast axis parallel to the main strain direction, however, other minerals such as pyroxene can have an opposite effect (fast axis perpendicular to the strain direction) and thus lower the observed bulk anisotropy (Barruol & Mainprice 1993; Silver 1996). In this work, we will apply the simplified assumption that the bulk LPO, and thus the anisotropic fast axis, is aligned parallel to the main strain direction.

5.5 Tectonic interpretation of the anisotropy pattern

The methodological uncertainties described above demand caution when interpreting the Ψ_2 anisotropic pattern. We will thus focus on areas where the potential bias is low (yellow bars in Figure 9). Our results indicate that in the valid model regions, the entire crust and uppermost mantle is affected by moderate levels (1 – 4%) of azimuthal anisotropy. This is different from recent results of the radially anisotropic structure which show anisotropy mostly underneath the Alpine and the Apenninic orogens (Alder et al. 2021). A comparison between our results and this study is difficult because of methodological differences and the different sensitivities of azimuthal and radial anisotropy to vertically/horizontally aligned fast axis.

The average principal stress direction in the Alps is N-S oriented except for the northern part of the western Alps and transition from eastern Alps to the Pannonian basin where an E-W orientation dominates (Fig. 1). According to the discussion above, we expect a parallel alignment of the fast axis direction with the principal stress direction at shallow depth. The shortest-period anisotropic measurements (3 – 5 s) have large uncertainties due to a stronger bias that make a conclusive comparison with the stress direction difficult. An agreement between principal stress direction and fast axis orientation is only visible in few parts of the map such as in parts of the central Alps and at the eastern edge of the eastern Alps. This may be due to the discussed methodological uncertainties, but the anisotropy may also be dominated by fault and fold structures instead of the stress field. In the eastern Alps, we infer from the higher phase velocities that the depth sensitivity of the Rayleigh waves should be deeper (Fig. S1) and thus the peak sensitivity may already lie below the 5 km estimate for the stress dominated anisotropic fast-axis alignment. A stress-related fast axis orientation at short periods is also proposed by Schippkus et al. (2018, 2019) who study the anisotropy in the Vienna basin region (Fig.

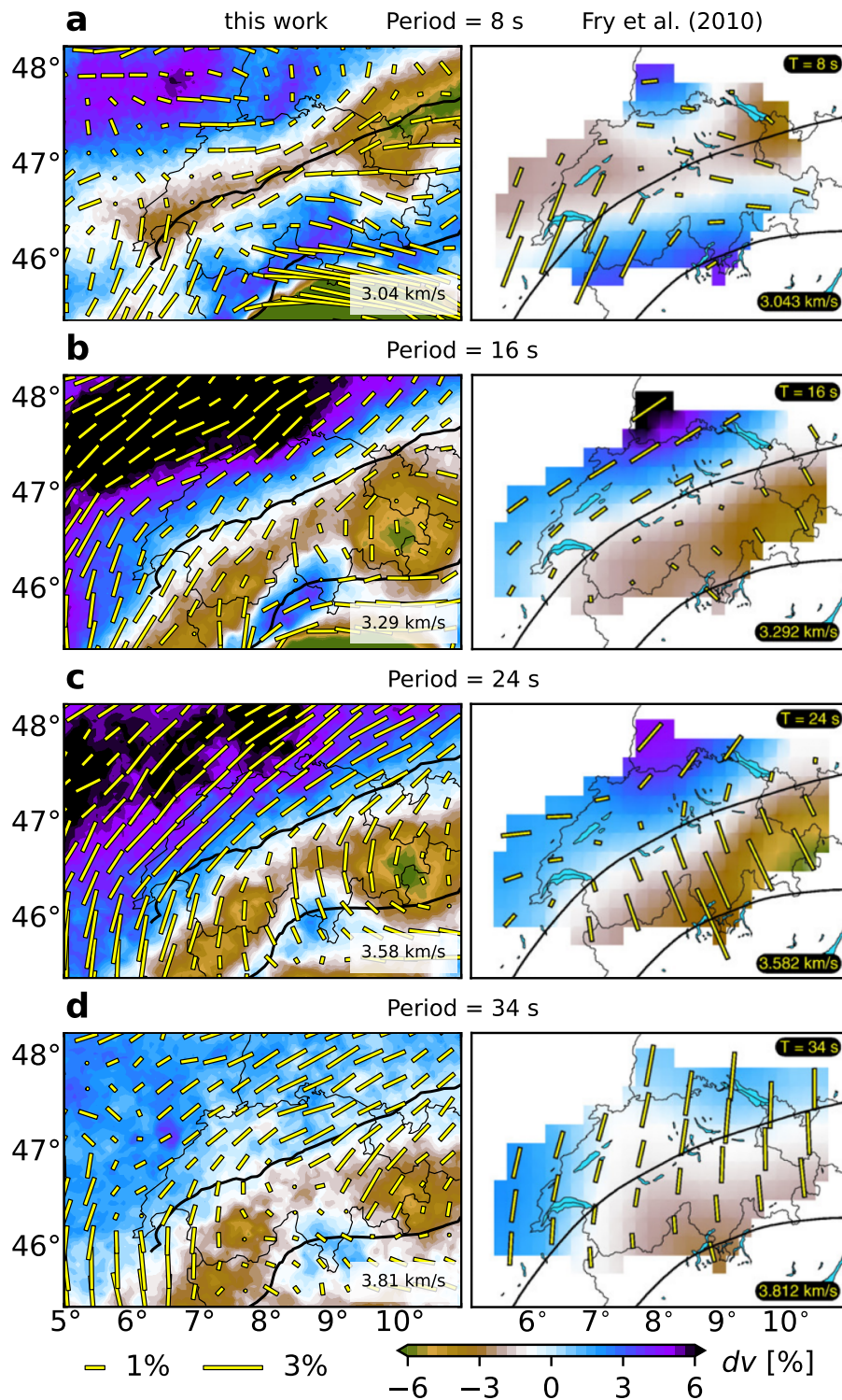


Figure 11. Comparison of the isotropic and anisotropic phase-velocity maps in Switzerland between this work (left panels) and the one of Fry et al. (2010, right panels) at four different periods **a** 8 s, **b** 16 s, **c** 24 s, **d** 34 s. The color model and the length of the anisotropic bars have been adapted to provide comparability between the models.

S12). A direct comparison between the studies is not possible, because Schippkus et al. (2019) use group velocities that have a different depth sensitivity; the strong velocity contrast to the adjacent low-velocity basin and the position at the edge of our model area limits the interpretability of the results in our study. The observed anisotropic fast axis curve around the low-velocity Vienna basin and are aligned in SW-NE direction within the basin correspond very well to the bias modeled in Figure 7 and are accordingly greyed out in Figure 9.

For the mid-to lower crustal depths, we can compare our results to the study of Fry et al. (2010) who image the azimuthal anisotropy in Switzerland at periods between 8 s and 40 s (Fig. 11). Both the isotropic and the anisotropic part are highly compatible between the two models up to a period of 24 s. In this period range, the fast axis are aligned roughly parallel to the arcuation of the Alpine orogen. Also in the western and northwestern foreland, this orientation can be observed (Fig. 9). This may be due to major thrust faults that formed the Alpine edifice but also other major lineaments such as the Periadriatic line (Fig. 1). Alternatively, LPO of crustal minerals due to compression (Fry et al. 2010) could cause this pattern. From 8 s to 24 s period (transition from mid to lower crust in the Alps), a change in fast axis orientation from arc-parallel to arc-perpendicular can be observed (Fry et al. 2010). The northern limit of the arc-perpendicular orientation at 16 s and 24 s coincides spatially with the Alpine front. It is interpreted by Fry et al. (2010) in terms of lower European crust which is uplifting in slices after European slab break-off and following slab retreat. In their model, this results in two displacement components, a vertical one, which is not imaged by the azimuthal anisotropy, and a northward one, which gives the arc-perpendicular orientation. This mechanism has been thermo-mechanically modeled showing both a northward and vertical component of the lower crustal stress tensor (Singer et al. 2014). According to our results, this process would be limited to the central Alps, as we do not observe a clear arc-perpendicular fast-axis orientation in the eastern or western Alps at periods between 20 – 30 s. This would be in agreement with models that suggest an attached slab in the central, but detached subduction slabs in the western and eastern Alps (Kästle et al. 2020; Paffrath et al. 2021; Handy et al. 2021).

In the eastern Alps, we expect to see an imprint of the eastward extrusion (Frisch et al. 1998) in the anisotropic fast-axis directions. Indeed, we observe higher, E-W oriented, anisotropic amplitudes between 3 – 20 s, compared to the rest of the Alps. The SEMP fault to the north, and the Periadriatic line to the south (Fig. 1) limit the extrusion area in agreement with the highest observed Ψ_2 amplitudes at 8 s and 12.5 s. We infer that the E-W pattern may be due to LPO of the minerals, parallel to the eastward motion. Above 12.5 s period, the E-W orientation is most prominent around the Periadriatic Fault zone which thus seems to affect the structure down to the lowermost crustal depths.

The measured Rayleigh waves start sampling the uppermost, lithospheric mantle above periods of about 20 s in the forelands, and 40 s in the Alps (sensitivity kernels in Fig. S1). This is largely controlled by the crustal thickness variations as can be seen from the lower velocities underneath the Alps, e.g. at 20 s period. Fry et al. (2010) find that at these periods, the fast axis in Switzerland orient consistently in N-S direction. We do not observe the same pattern, instead the images in Figure 11 suggest a continuation of the arc-parallel anisotropic fast axis orientation in the western and northern Alpine foreland up to approx. 50 s. The arc-parallel foreland structure can be followed eastwards to about 13^{circ}E where they turn northwards. This coincides spatially with the border to the Bohemian Massif (Fig. 1). We infer thus that there may be LPO orientation in the uppermost, lithospheric mantle in the European plate. The herein presented results are compared to those obtained with Pn waves (sensitive to the uppermost mantle; Diaz et al. 2013) and a compilation of SKS results (most sensitive to the upper mantle; Wüstefeld et al. 2009, and references therein) in Figure 12. At 20 s period, the fast axis orientations in the northern Alpine foreland are highly compatible between Pn- and surface-wave results, including the arc-parallel flow that turns northward at approx. 10°E . Within the Alps, the 20 s surface-waves are mostly sampling the lowermost crustal structure and therefore Pn results and those from this work do not match well. SKS waves are sensitive to deeper structure and thus we see the best compatibility for long periods surface waves (Fig. 12). Both methods show the well known flow field around the western Alps and the arc-parallel orientation under the Alps and underneath both southern and northern forelands (Wüstefeld et al. 2009; Barruol et al. 2011; Salimbeni et al. 2018; Petrescu et al. 2020). The herein presented surface-wave results thus help to better understand the depth-sensitivity of SKS splitting studies in the Alpine region.

6 CONCLUSIONS

We extract phase-dispersion curves from ambient-noise cross correlations for two years of AlpArray data. The resulting Rayleigh-wave phase-velocity measurements are used to obtain azimuthally anisotropic maps at periods between 3s and 80s with the Eikonal tomography method.

Through a suite of synthetic tests, we illustrate how strong velocity variations may bias the mapped anisotropy. We attribute the bias to two mechanisms: (1) finite frequency effects that directly affect the phase velocity measurements between station pairs. These are caused by low-velocity zones that can produce a secondary wavefront downstream from the velocity anomaly and interference between direct and reflected/refracted and/or multiple waves. These produced artifacts are period-dependent and can be significantly reduced if the amplitude information is taken into account (Helmholtz tomography). This is, however, only possible if good amplitude information at densely spaced sample (i.e. station)

locations is available. (2) artifacts due to incomplete sampling of the travel-time field. This problem is most pronounced at short periods where the wavefront is very complex and thus only a smoothed and distorted travel-time field can be recovered. We show that at short periods (relative to the inter-station spacing and the strength of the wavefield distortion due to velocity heterogeneities), the under-sampling is responsible for most of the reported bias.

The spurious Ψ_2 anisotropy appears most prominent within low-velocity regions and at the borders of large velocity contrasts. For the shown application to the AlpArray network with typical station spacing of 50 km, a bias from velocity heterogeneities of $\pm 10\%$ and less seems negligible, at the herein studied periods. In the isotropic velocity distribution, most of the bias cancels out, given that there is good azimuthal coverage.

We find that the anisotropic bias has a rough spatial correlation with the amplitude of the Ψ_1 anisotropy and the mapped uncertainty in A_2 , with the latter being more consistent. We therefore use the A_2 uncertainty as indicator for potentially biased regions in our final maps and we exclude anisotropy estimates for those regions from our final maps. For the remaining regions in the real data maps we interpret the anisotropic structures as follows:

- At mid-crustal depths, an E-W orientation of the anisotropic fast axis is observed in the entire Alpine arc. This could be explained with the orientation of major faults and lineaments and the LPO of crystals due to compression as proposed by Fry et al. (2010).
- In the lower crust, an arc-perpendicular pattern emerges in the central Alps. In the eastern Alps, the pattern remains rather E-W oriented. We interpret the consistent E-W orientation in the eastern Alps as imprint of the eastward extrusion and find the most pronounced effect on the anisotropic fast axis around the eastern Periadriatic Fault zone.
- In the northern Alpine foreland a simple, arc-parallel pattern of fast axis becomes visible at lower crustal and uppermost mantle depths, limited in the east by the Bohemian Massif. This orientation is similar to the one observed from Pn waves and in SKS studies and is probably related to the Alpine orogeny.

ACKNOWLEDGMENTS

We want to thank the editor Huajian Yao and the two reviewers, Lili Feng and Weisen Shen, for their insightful comments that helped to improve this manuscript. The authors are grateful to the AlpArray Seismic Network Team (www.alparray.ethz.ch/seismic_network/backbone/management). Data processing was done with the Python software *ants_2* provided by L. Ermert (github.com/lermert/ants_2) and Obspy (Beyreuther et al. 2010). We want to thank the HPC services of the geophysi-

cal department of the ETH Zurich and of the ZEDAT, Freie Universität Berlin for the computational resources (Bennett et al. 2020). The synthetic simulations are based on the scikit-fmm software (github.com/scikit-fmm/scikit-fmm) and Devito (www.devitoproject.org; Luporini et al. 2018; Louboutin et al. 2019). The synthetic model is based on a satellite image provided by ESA (www.esa.int). EK has received funding from the German Science Foundation (SPP-2017, Project Ha 2403/21-1). IM carried out this work within the Swiss National Science Foundation SINERGIA Project CRSII2-154434/1 (Swiss-AlpArray) and the Progetto Pianeta Dinamico, finanziamento MUR-INGV, Task S2 – 2021.

DATA AVAILABILITY

The data from the AlpArray experiment is distributed through ORFEUS and EIDA (www.orfeus-eu.org/data/eida/) and freely accessible to all AlpArray Working Group members (www.alparray.ethz.ch/en/organisation/partecipants/). The data will become publicly accessible by March 2022. The AlpArray Seismic Network comprises the temporary AlpArray stations (Z3 2015) and the following permanent networks: BW (2001); CH (1983); CR (2001); CZ (1973); FR (1995); HU (1992); G (1982); GE (1993); GR (1976); GU (1967); HS (2012); IU (1988); NI (2002); OE (1987); OX (2016); RD (2018); RF (1993); SK (2004); SL (2001); ST (1981); SX (2001); TH (2009).

REFERENCES

- Aki, K., 1957. Space and time spectra of stationary stochastic waves, with special reference to microtremors, *Bulletin of the Earthquake Research Institute, University of Tokyo*, **35**(3), 415–456.
- Alder, C., Debayle, E., Bodin, T., Paul, A., Stehly, L., Pedersen, H., et al., 2021. Evidence for radial anisotropy in the lower crust of the apennines from bayesian ambient noise tomography in europe, *Geophysical Journal International*.
- Barruol, G. & Mainprice, D., 1993. 3-D seismic velocities calculated from lattice-preferred orientation and reflectivity of a lower crustal section: examples of the Val Sesia section (Ivrea zone northern Italy), *Geophysical Journal International*, **115**(3), 1169–1188.
- Barruol, G., Bonnin, M., Pedersen, H., Bokelmann, G. H., & Tiberi, C., 2011. Belt-parallel mantle flow beneath a halted continental collision: The Western Alps, *Earth and Planetary Science Letters*, **302**(3-4), 429–438.
- Bennett, L., Melchers, B., & Proppe, B., 2020. Curta: A General-purpose High-Performance Computer at ZEDAT, Freie Universität Berlin, Tech. rep., Freie Universität Berlin.
- Beyreuther, M., Barsch, R., Krischer, L., Megies, T., Behr, Y., & Wassermann, J., 2010. ObsPy: A Python Toolbox for Seismology, *Seismological Research Letters*, **81**(3), 530–533.

- Bodin, T. & Maupin, V., 2008. Resolution potential of surface wave phase velocity measurements at small arrays, *Geophysical Journal International*, **172**(2), 698–706.
- Boschi, L. & Dziewonski, A. M., 1999. High- and low-resolution images of the Earth's mantle: Implications of different approaches to tomographic modeling, *Journal of Geophysical Research: Solid Earth*, **104**(B11), 25567–25594.
- Boue, P., Poli, P., Campillo, M., Pedersen, H., Briand, X., & Roux, P., 2013. Teleseismic correlations of ambient seismic noise for deep global imaging of the Earth, *Geophysical Journal International*, **194**(2), 844–848.
- BW, 2001. Bayernnetz, Tech. rep., Department Of Earth And Environmental Sciences, Geophysical Observatory, University Of Munchen.
- Carminati, E., Lustrino, M., & Doglioni, C., 2012. Geodynamic evolution of the central and western Mediterranean: Tectonics vs. igneous petrology constraints, *Tectonophysics*, **579**, 173–192.
- CH, 1983. National seismic networks of Switzerland, Tech. rep., Swiss Seismological Service (SED) At ETH Zurich.
- CR, 2001. Croatian seismograph network, Tech. rep., University Of Zagreb.
- Crampin, S., 1994. The fracture criticality of crustal rocks, *Geophysical Journal International*, **118**(2), 428–438.
- CZ, 1973. Czech regional seismic network, Tech. rep., Institute Of Geophysics, A. O. S. O. T. C. R.
- de Ridder, S. & Dellinger, J., 2011. Ambient seismic noise eikonal tomography for near-surface imaging at Valhall, *The Leading Edge*, **30**(5), 506–512.
- Diaz, J., Gil, A., & Gallart, J., 2013. Uppermost mantle seismic velocity and anisotropy in the Euro-Mediterranean region from Pn and Sn tomography, *Geophysical Journal International*, **192**(1), 310–325.
- Dziewonski, A. M., Chou, T.-A., & Woodhouse, J. H., 1981. Determination of earthquake source parameters from waveform data for studies of global and regional seismicity, *Journal of Geophysical Research: Solid Earth*, **86**(B4), 2825–2852.
- Ekström, G., 2001. Time domain analysis of Earth's long-period background seismic radiation, *Journal of Geophysical Research: Solid Earth*, **106**(B11), 26483–26493.
- Ekström, G., Abers, G. A., & Webb, S. C., 2009. Determination of surface-wave phase velocities across USArray from noise and Akis spectral formulation, *Geophysical Research Letters*, **36**(18).
- Ekström, G., Nettles, M., & Dziewoński, A., 2012. The global CMT project 2004–2010: Centroid-moment tensors for 13,017 earthquakes, *Physics of the Earth and Planetary Interiors*, **200-201**, 1–9.
- Feng, L. & Ritzwoller, M. H., 2017. The effect of sedimentary basins on surface waves that pass through them, *Geophysical Journal International*, **211**(1), 572–592.
- Fichtner, A., Bowden, D., & Ermer, L., 2020. Optimal processing for seismic noise correlations, *Geophysical Journal International*, **223**(3), 1548–1564.
- FR, 1995. Resif-rlbp French broad-band network, resif-rap strong motion network and other seismic stations in metropolitan France, Tech. rep., RESIF - Réseau Sismologique et Géologique Français.

- Franke, W., Cocks, L. R. M., & Torsvik, T. H., 2017. The palaeozoic variscan oceans revisited, *Gondwana Research*, **48**, 257–284.
- Friederich, W., Hunzinger, S., & Wielandt, E., 2000. A note on the interpretation of seismic surface waves over three - dimensional structures, *Geophysical Journal International*, **143**(2), 335–339.
- Frisch, W., Kuhlemann, J., Dunkl, I., & Brgel, A., 1998. Palinspastic reconstruction and topographic evolution of the Eastern Alps during late Tertiary tectonic extrusion, *Tectonophysics*, **297**(1-4), 1–15.
- Fry, B., Deschamps, F., Kissling, E., Stehly, L., & Giardini, D., 2010. Layered azimuthal anisotropy of Rayleigh wave phase velocities in the European Alpine lithosphere inferred from ambient noise, *Earth and Planetary Science Letters*, **297**(1-2), 95–102.
- G, 1982. Geoscope, french global network of broad band seismic stations, Tech. rep., Institut De Physique Du Globe De Paris (IPGP), & Ecole Et Observatoire Des Sciences De La Terre De Strasbourg (EOST).
- Gallego, A., Panning, M., Russo, R., Comte, D., Mocanu, V., Murdie, R., & Vandecar, J., 2011. Azimuthal anisotropy in the Chile Ridge subduction region retrieved from ambient noise, *Lithosphere*, **3**(6), 393–400.
- GE, 1993. Geofon seismic network, Tech. rep., GEOFON Data Centre and Deutsches GeoForschungsZentrum GFZ.
- GR, 1976. German regional seismic network (grsn). bundesanstalt fr geowissenschaften und rohstoffe, Tech. rep., Federal Institute for Geosciences and Natural Resources.
- GU, 1967. Regional seismic network of north western italy, Tech. rep., University Of Genoa.
- Guo, Z., Gao, X., Yao, H., & Wang, W., 2017. Depth variations of azimuthal anisotropy beneath the Tian Shan Mt range (NW China) from ambient noise tomography, *Journal of Asian Earth Sciences*, **138**, 161–172.
- Handy, M., Schmid, S., Paffrath, M., Friederich, W., Group, A. W., et al., 2021. European tectosphere and slabs beneath the greater alpine area—interpretation of mantle structure in the alps-apennines-pannonian region from teleseismic v p studies, *Solid Earth Discussions*, pp. 1–61.
- Handy, M. R., Schmid, S. M., Bousquet, R., Kissling, E., & Bernoulli, D., 2010. Reconciling plate-tectonic reconstructions of Alpine Tethys with the geological–geophysical record of spreading and subduction in the Alps, *Earth-Science Reviews*, **102**(3-4), 121–158.
- Handy, M. R., Ustaszewski, K., & Kissling, E., 2014. Reconstructing the Alps–Carpathians–Dinarides as a key to understanding switches in subduction polarity slab gaps and surface motion, *International Journal of Earth Sciences*, **104**(1), 1–26.
- Heidbach, O., Rajabi, M., Reiter, K., Ziegler, M., & Team, W., 2016. World Stress Map Database Release 2016 V. 1.1, <https://doi.org/10.5880/WSM.2016.001>.
- Hetényi, G., Molinari, I., Clinton, J., Bokelmann, G., Bondár, I., Crawford, W. C., Dessa, J.-X., Doubre, C., Friederich, W., Fuchs, F., Giardini, D., Grácz, Z., Handy, M. R., Herak, M., Jia, Y., Kissling, E., Kopp, H., Korn, M., Margheriti, L., Meier, T., Mucciarelli, M., Paul, A., Pesaresi, D., Piromallo, C., Plenefisch, T., Plomerová, J., Ritter, J., Rmpker, G., Šipka, V., Spallarossa, D., Thomas, C., Tilmann, F., Wassermann, J., Weber, M., Wéber, Z., Wesztergom, V., Živčić, M., & and, 2018. The AlpArray Seismic Network: A Large-Scale European Experiment to Image the Alpine Orogen, *Surveys in Geophysics*, **39**(5), 1009–1033.

- HS, 2012. Hessischer erdbebendienst, Tech. rep., Hessian Agency For Nature Conservation, Environment And Geology.
- HU, 1992. Hungarian national seismological network, Tech. rep., Kvesligethy Rad Seismological Observatory (Geodetic And Geophysical Institute, Research Centre For Astronomy And Earth Sciences, Hungarian Academy Of Sciences (MTA CSFK GGI KRSZO)).
- IU, 1988. Global seismograph network (gsn - iris/usgs)., Tech. rep., Albuquerque Seismological Laboratory (ASL)/USGS.
- Kern, H., 1990. Laboratory seismic measurements: an aid in the interpretation of seismic field data, *Terra Nova*, **2**(6), 617–628.
- Kern, H. & Schmidt, R., 1990. Physical properties of KTB core samples at simulated in situ conditions, *Scientific Drilling*, **1**(5), 217–223.
- Kissling, E. & Schlunegger, F., 2018. Rollback orogeny model for the evolution of the swiss alps, *Tectonics*, **37**(4), 1097–1115.
- Kstle, E. D., Soomro, R., Weemstra, C., Boschi, L., & Meier, T., 2016. Two-receiver measurements of phase velocity: cross-validation of ambient-noise and earthquake-based observations, *Geophysical Journal International*, **207**(3), 1493–1512.
- Kstle, E. D., El-Sharkawy, A., Boschi, L., Meier, T., Rosenberg, C., Bellahsen, N., Cristiano, L., & Weidle, C., 2018. Surface Wave Tomography of the Alps Using Ambient-Noise and Earthquake Phase Velocity Measurements, *Journal of Geophysical Research: Solid Earth*, **123**(2), 1770–1792.
- Kstle, E. D., Rosenberg, C., Boschi, L., Bellahsen, N., Meier, T., & El-Sharkawy, A., 2020. Slab break-offs in the Alpine subduction zone, *International Journal of Earth Sciences*, **109**(2), 587–603.
- Lehuteur, M. & Chevrot, S., 2020. On the validity of the eikonal equation for surface-wave phase-velocity tomography, *Geophysical Journal International*, **223**(2), 908–914.
- Lin, F.-C. & Ritzwoller, M. H., 2011a. Helmholtz surface wave tomography for isotropic and azimuthally anisotropic structure, *Geophysical Journal International*, **186**(3), 1104–1120.
- Lin, F.-C. & Ritzwoller, M. H., 2011b. Apparent anisotropy in inhomogeneous isotropic media, *Geophysical Journal International*, **186**(3), 1205–1219.
- Lin, F.-C., Ritzwoller, M. H., & Snieder, R., 2009. Eikonal tomography: surface wave tomography by phase front tracking across a regional broad-band seismic array, *Geophysical Journal International*, **177**(3), 1091–1110.
- Lin, F.-C., Li, D., Clayton, R. W., & Hollis, D., 2013. High-resolution 3D shallow crustal structure in Long Beach California: Application of ambient noise tomography on a dense seismic array, *GEOPHYSICS*, **78**(4), Q45–Q56.
- Louboutin, M., Lange, M., Luporini, F., Kukreja, N., Witte, P. A., Herrmann, F. J., Velesko, P., & Gorman, G. J., 2019. Devito (v3.1.0): an embedded domain-specific language for finite differences and geophysical exploration, *Geoscientific Model Development*, **12**(3), 1165–1187.
- Lschen, E., Sllner, W., Hohrath, A., & Rabbel, W., 1991. Integrated P- and S-wave borehole experiments at

- the KTB-deep drilling site in the Oberpfalz area (SE Germany), in *Continental Lithosphere: Deep Seismic Reflections*, pp. 121–133, American Geophysical Union.
- Lu, Y., 2019. *Tomography of the alpine arc using noise correlations waveform modelling*, Ph.D. thesis, Université Grenoble Alpes.
- Lu, Y., Stehly, L., & and, A. P., 2018. High-resolution surface wave tomography of the European crust and uppermost mantle from ambient seismic noise, *Geophysical Journal International*, **214**(2), 1136–1150.
- Luporini, F., Lange, M., Louboutin, M., Kukreja, N., Hükelheim, J., Yount, C., Witte, P., Kelly, P. H. J., Herrmann, F. J., & Gorman, G. J., 2018. Architecture and performance of devito, a system for automated stencil computation, *CoRR*, **abs/1807.03032**.
- Malusà, M. G., Faccenna, C., Baldwin, S. L., Fitzgerald, P. G., Rossetti, F., Balestrieri, M. L., Danišík, M., Ellero, A., Ottria, G., & Piromallo, C., 2015. Contrasting styles of (u) hp rock exhumation along the cenozoic adria-europe plate boundary (western alps, calabria, corsica), *Geochemistry, Geophysics, Geosystems*, **16**(6), 1786–1824.
- Mordret, A., Shapiro, N. M., Singh, S. S., Roux, P., & Barkved, O. I., 2013. Helmholtz tomography of ambient noise surface wave data to estimate Scholte wave phase velocity at Valhall Life of the Field, *GEOPHYSICS*, **78**(2), WA99–WA109.
- NI, 2002. North-east italy broadband network, Tech. rep., OGS (Istituto Nazionale Di Oceanografia E Di Geofisica Sperimentale) And University Of Trieste.
- Nicolas, A. & Christensen, N. I., 1987. Formation of anisotropy in upper mantle peridotites: A review, in *Composition Structure and Dynamics of the Lithosphere-Asthenosphere System*, pp. 111–123, American Geophysical Union.
- Nolet, G. & Dahlen, F. A., 2000. Wave front healing and the evolution of seismic delay times, *Journal of Geophysical Research: Solid Earth*, **105**(B8), 19043–19054.
- OE, 1987. Austrian seismic network, Tech. rep., ZAMG-Zentralanstalt Fr Meteorologie Und Geodynamik.
- OX, 2016. North-east italy seismic network, Tech. rep., OGS (Istituto Nazionale Di Oceanografia E Di Geofisica Sperimentale).
- Paffrath, M., Friederich, W., AlpArray, working group, A.-S. D., et al., 2021. Imaging structure and geometry of slabs in the greater alpine area—a p-wave traveltimes tomography using alparray seismic network data, *Solid Earth Discussions*, pp. 1–40.
- Petrescu, L., Pondrelli, S., Salimbeni, S., Faccenda, M., Group, A. W., et al., 2020. Mantle flow below the central and greater alpine region: insights from sks anisotropy analysis at alparray and permanent stations, *Solid Earth*, **11**(4), 1275–1290.
- Qorbani, E., Bianchi, I., & Bokelmann, G., 2015. Slab detachment under the Eastern Alps seen by seismic anisotropy, *Earth and Planetary Science Letters*, **409**, 96–108.
- RD, 2018. Cea/dase broad-band permanent network in metropolitan france, Tech. rep., RESIF - Réseau Sismologique et Géologique Français.
- RF, 1993. Friuli venezia giulia accelerometric network, Tech. rep., University Of Trieste.

- Salimbeni, S., Malusà, M. G., Zhao, L., Guillot, S., Pondrelli, S., Margheriti, L., Paul, A., Solarino, S., Aubert, C., Dumont, T., et al., 2018. Active and fossil mantle flows in the western alpine region unravelled by seismic anisotropy analysis and high-resolution p wave tomography, *Tectonophysics*, **731**, 35–47.
- Scharf, A., Handy, M., Favaro, S., Schmid, S. M., & Bertrand, A., 2013. Modes of orogen-parallel stretching and extensional exhumation in response to microplate indentation and roll-back subduction (tauern window, eastern alps), *International Journal of Earth Sciences*, **102**(6), 1627–1654.
- Schippkus, S., Zigone, D., Bokelmann, G., & the AlpArray Working Group, 2018. Ambient-noise tomography of the wider Vienna Basin region, *Geophysical Journal International*, **215**(1), 102–117.
- Schippkus, S., Zigone, D., Bokelmann, G., Hetényi, G., Abreu, R., Allegretti, I., Apoloner, M.-T., Aubert, C., Besançon, S., Berc, M. B. D., Bokelmann, G., Brunel, D., Capello, M., Čarman, M., Cavaliere, A., Chèze, J., Chiarabba, C., Clinton, J., Cougoulat, G., Crawford, W. C., Cristiano, L., Czifra, T., Dalema, E., Danesi, S., Daniel, R., Dannowski, A., Dasović, I., Deschamps, A., Dessa, J.-X., Doubre, C., Egdorf, S., Fiket, T., Fischer, K., Friederich, W., Fuchs, F., Funke, S., Giardini, D., Govoni, A., Gráczner, Z., Grschl, G., Heimers, S., Heit, B., Herak, D., Herak, M., Huber, J., Jarić, D., Jedlička, P., Jia, Y., Jund, H., Kissling, E., Klingen, S., Klotz, B., Kolínský, P., Kopp, H., Korn, M., Kotek, J., Khne, L., Kuk, K., Lange, D., Loos, J., Lovati, S., Malengros, D., Margheriti, L., Maron, C., Martin, X., Massa, M., Mazzarini, F., Meier, T., Métral, L., Molinari, I., Moretti, M., Munzarová, H., Nardi, A., Pahor, J., Paul, A., Péquegnat, C., Petersen, D., Pesaresi, D., Piccinini, D., Piromallo, C., Plenefisch, T., Plomerová, J., Pondrelli, S., Prevolnik, S., Racine, R., Régnier, M., Reiss, M., Ritter, J., Rmpker, G., Salimbeni, S., Santulin, M., Scherer, W., Schippkus, S., Schulte-Kortnack, D., v Šipka, Solarino, S., Spallarossa, D., Spieker, K., Stipčević, J., Strollo, A., Sle, B., Szanyi, G., Szcs, E., Thomas, C., Thorwart, M., Tilmann, F., Ueding, S., Vallocchia, M., Vecsey, L., Voigt, R., Wassermann, J., Wéber, Z., Weidle, C., v Westergom, Weyland, G., Wiemer, S., Wolf, F., Wolyniec, D., Zieke, T., Živčić, M., & and, 2019. Azimuthal anisotropy in the wider Vienna basin region: a proxy for the present-day stress field and deformation, *Geophysical Journal International*, **220**(3), 2056–2067.
- Schmid, S. M., Fgenschuh, B., Kissling, E., & Schuster, R., 2004. Tectonic map and overall architecture of the Alpine orogen, *Eclogae Geologicae Helvetiae*, **97**(1), 93–117.
- Schmid, S. M., Bernoulli, D., Fgenschuh, B., Matenco, L., Schefer, S., Schuster, R., Tischler, M., & Ustaszewski, K., 2008. The Alpine-Carpathian-Dinaridic orogenic system: correlation and evolution of tectonic units, *Swiss Journal of Geosciences*, **101**(1), 139–183.
- Schulmann, K. & Gayer, R., 2000. A model for a continental accretionary wedge developed by oblique collision: the ne bohemian massif, *Journal of the Geological Society*, **157**(2), 401–416.
- Shearer, P. M., 2009. *Introduction to Seismology*, Cambridge University Press.
- Silver, P. G., 1996. SEISMIC ANISOTROPY BENEATH THE CONTINENTS: Probing the Depths of Geology, *Annual Review of Earth and Planetary Sciences*, **24**(1), 385–432.
- Singer, J., Diehl, T., Husen, S., Kissling, E., & Duretz, T., 2014. Alpine lithosphere slab rollback causing lower crustal seismicity in northern foreland, *Earth and Planetary Science Letters*, **397**, 42–56.
- SK, 2004. National network of seismic stations of slovakia, Tech. rep., ESI SAS (Earth Science Institute Of

- The Slovak Academy Of Sciences).
- SL, 2001. Seismic network of the republic of slovenia, Tech. rep., Slovenian Environment Agency.
- Smith, M. L. & Dahlen, F. A., 1973. The azimuthal dependence of Love and Rayleigh wave propagation in a slightly anisotropic medium, *Journal of Geophysical Research*, **78**(17), 3321–3333.
- Smith, W. H. F. & Wessel, P., 1990. Gridding with continuous curvature splines in tension, *GEOPHYSICS*, **55**(3), 293–305.
- ST, 1981. Trentino seismic network, Tech. rep., Geological Survey-Provincia Autonoma Di Trento.
- SX, 2001. Sxnet saxon seismic network, Tech. rep., Leipzig University.
- TH, 2009. Thringer seismologisches netz (tsn), Tech. rep., Jena, F. S. U.
- Tsai, V. C., 2009. On establishing the accuracy of noise tomography travel-time measurements in a realistic medium, *Geophysical Journal International*, **178**(3), 1555–1564.
- Verwater, V. F., Le Breton, E., Handy, M. R., Picotti, V., Jozi Najafabadi, A., & Haberland, C., 2021. Neogene kinematics of the giudicarie belt and eastern southern alpine orogenic front (northern italy), *Solid Earth*, **12**(6), 1309–1334.
- Weaver, R., Froment, B., & Campillo, M., 2009. On the correlation of non-isotropically distributed ballistic scalar diffuse waves, *The Journal of the Acoustical Society of America*, **126**(4), 1817.
- Wielandt, E., 1993. Propagation and Structural Interpretation of Non-Plane Waves, *Geophysical Journal International*, **113**(1), 45–53.
- Wüstefeld, A., Bokelmann, G., Barruol, G., & Montagner, J.-P., 2009. Identifying global seismic anisotropy patterns by correlating shear-wave splitting and surface-wave data, *Physics of the Earth and Planetary Interiors*, **176**(3-4), 198–212.
- Xu, H., Luo, Y., Chen, C., & Xu, Y., 2016. 3D shallow structures in the Baogutu area Karamay, determined by eikonal tomography of short-period ambient noise surface waves, *Journal of Applied Geophysics*, **129**, 101–110.
- Yang, Y. & Ritzwoller, M. H., 2008. Characteristics of ambient seismic noise as a source for surface wave tomography, *Geochemistry Geophysics, Geosystems*, **9**(2), n/a–n/a.
- Yao, H. & van der Hilst, R. D., 2009. Analysis of ambient noise energy distribution and phase velocity bias in ambient noise tomography with application to SE Tibet, *Geophysical Journal International*, **179**(2), 1113–1132.
- Z3, 2015. Alpparray seismic network (2015): Alpparray seismic network (aasn) temporary component., Tech. rep., AlpArray Working group.
- Zhao, L., Paul, A., Guillot, S., Solarino, S., Malusà, M. G., Zheng, T., Aubert, C., Salimbeni, S., Dumont, T., Schwartz, S., et al., 2015. First seismic evidence for continental subduction beneath the western alps, *Geology*, **43**(9), 815–818.

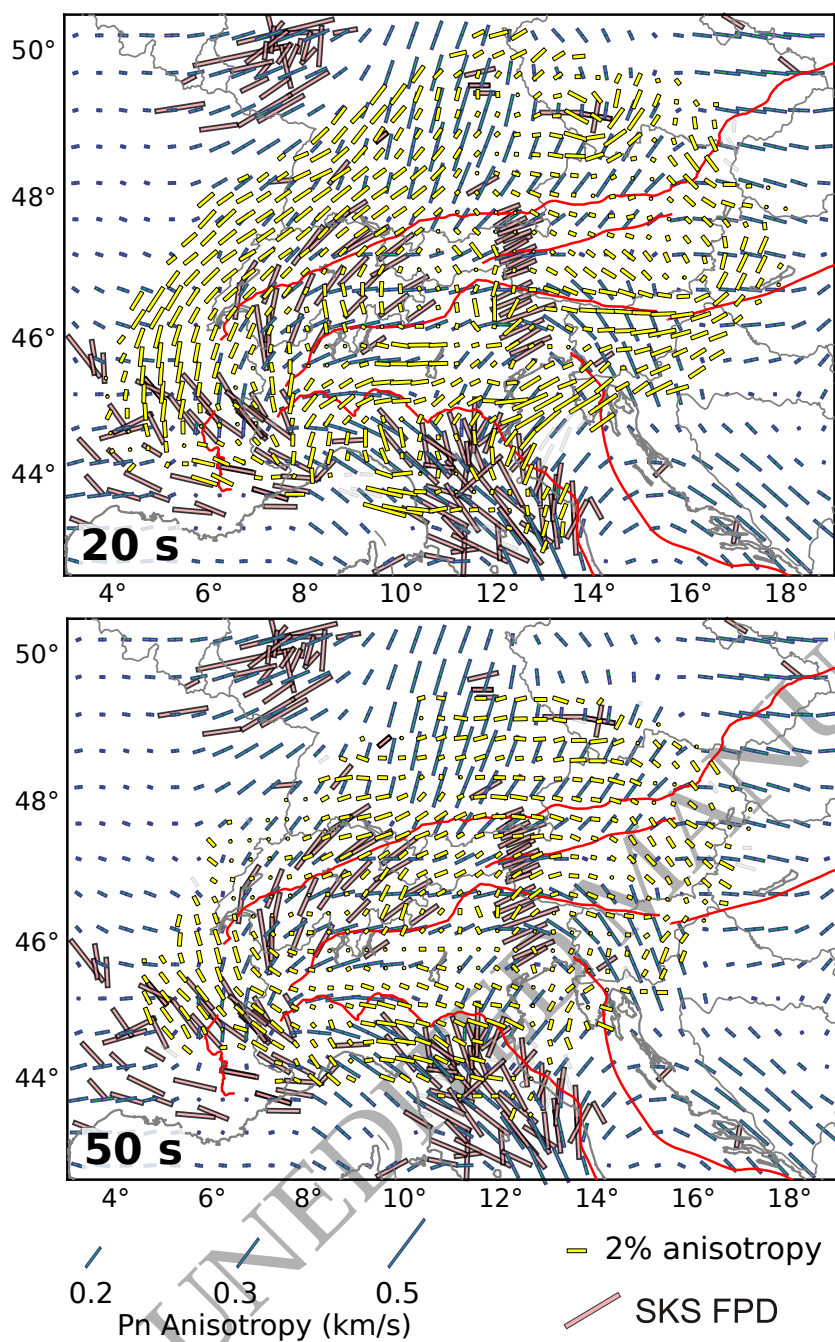


Figure 12. Comparison between Pn anisotropy from Diaz et al. (2013, blue bars), a compilation of SKS fast propagation directions (SKS FPD, light red bars) modified from Wüstefeld et al. (2009); Diaz et al. (2013) and the anisotropic fast-axis results from this work (yellow bars) at 20 s and 50 s period. The red lines indicate major tectonic lineaments (Fig. 1).